8-2013

Design of a Compliant Underactuated Robotic Finger with Coordinated Stiffness

Etienne Dessauw
University of Nebraska-Lincoln, etienne-59@hotmail.fr

Design of a Compliant Underactuated Robotic Finger with Coordinated Stiffness

by

Etienne Dessauw

A THESIS

Presented to the Faculty of

The Graduate College at the University of Nebraska

In Partial Fulfillment of Requirements

For the Degree of Master of Science

Major: Mechanical Engineering and Applied Mechanics

Under the Supervision of Professor Carl A. Nelson

Lincoln, Nebraska

August, 2013

Design of a Compliant Underactuated Robotic Finger with Coordinated Stiffness

Etienne Dessauw, M.S.

University of Nebraska, 2013

Advisor: Carl A. Nelson

The concept of underactuation has been previously developed in the robotic field for grasping applications. For these anthropomorphic grippers, the minimization of the number of input signals, or in other words underactuation, is the most expected characteristic. This method has become very popular in recent decades. Indeed, by minimizing the number of input signals, it minimizes the complexity of the system's control and at the same time avoids increased weight and cost. The inconvenience of such a technique is that the design of this type of system remains a difficult task if the behavior of the underactuated set of joints is to remain within certain constraints.

In this thesis, an underactuated robotic finger whose grasping behavior is modulated by the design of its superelastic joints is proposed. Using shape-memory alloy, the finger joints can be given specific stiffness and pre-form shapes such that a single-cable actuation rather than opposing-pair actuation can be used; this also allows the grasping motions of the phalanges to be synchronized in the free phase and then adaptive once contact is made. A default-closed pre-tensioned configuration allows grasp forces to be maximal for larger objects and still keeps control components such as tendons out of the grasp workspace. The simplicity of the design lends itself to the possibility of integrated joint angle and surface pressure sensing on the finger itself. The details of design, prototyping and testing are described.

Acknowledgements

I would like to particularly thank Professor Nelson for giving me the opportunity to work with him on this captivating project and for his great assistance all along the development of the prototype, the preparation of this thesis and the writing of the related published paper. Thank you to Professor Saiter, Professor Negahban and the staff of the both universities (University of Rouen and UNL) without whom this student's exchange program wouldn't have been possible. I would also like to thank everyone in the lab for their help and for their welcome; it has been a pleasure to work with you over this year. I finally would like to thank my family who has been tremendously supportive over my university education and my entire life; I'll soon be able to stand on my two feet. Without forgetting my second family with whom I almost spent 2 years of my life. Thank you to Emilie, Benjamin and Quentin. This experience wouldn't have been the same without you.

Table of Contents

List of Figures

List of Tables

Chapter 1: Introduction

In recent years, researchers have focused on the development and manufacture of more and more sophisticated humanoid robotic hands/fingers. Due to the complexity of the human hand, many different robotic variations are possible, depending on the application(s) the hand/finger is made for. Many features need to be considered from different fields: the size, shape and other dimensional aspects of the robotic hand, but most importantly, the degrees of freedom (DOFs) and kinematic topology, the grasping force and the method of controlling this force in such a way as to adapt it to the desired grasping object. Robotic hand mechanisms can be generalized into two main classes: fully actuated dexterous mechanisms and underactuated robotic mechanisms.

Fully actuated robotic dexterous hands are able to closely mimic the functionality of a humanoid hand thanks to a combination of actuators, sensors and control systems and other components. On the other hand, such structures have drawbacks such as complexity, higher weight, and increased cost. Nevertheless, a number of reliable dexterous hands have been realized: DLR Hands I and II (Germany) [1, 2], the Shadow Dexterous Hand C6M2 (England) [3], the Utah/MIT dexterous hand (United States) [4] and also the DEKA hand [5].

Secondly, much attention has been given to underactuated mechanical systems. These are systems whose number of control inputs is less than their overall number of DOF [6]. These kinds of systems have the advantages of simplified structure, reduced volume, light weight and lower cost. Also, by reducing the number of inputs (actuators) [7], the hand's capability to adapt its shape to the grasped object may be enhanced. Examples of such mechanisms are the TUAT/Karlsruhe Humanoid Hand (Japan/Germany) [8], the multifingered self-adaptive hand of Rakic [9], Graspar [10], and the SDM Hand [11]. In some cases, researchers have focused more specifically on the design of underactuated fingers [12].

The design of a fully compliant underactuated robotic finger is described in the remainder of this Thesis. The concept of the underactuated hand is adapted to further reduce complexity and enable good grasping contact with objects of arbitrary convex geometry. The thesis is organized in chapters: the first two chapters provide background on related robotic mechanisms, which are very important to fully understand the definition and characteristics of underactuated mechanisms. The third chapter explains the conceptual idea of the prototype, based on some of the characteristics of a well-known underactuated hand, the Shadow Dexterous Hand. The fourth and fifth chapters address the choice and characterization of the materials for prototyping the finger. Chapter six focuses on the tests performed on the prototype to confirm the functionality of the design compared to the theory and also to verify the suitability of the chosen materials.

Chapter 2: Robotic Background

Robotic grasping systems can be differentiated into categories. Depending on the features and the applications that the robot is designed for, in this case a robotic hand, we can split up in two categories: humanoid dexterous robotic hands and underactuated mechanical hands. The differences between both will be described in the following sections.

2.1. Humanoid dexterous hands

The humanoid dexterous hand can be considered one of the most significant technological breakthroughs in robotics. The purpose of this kind of research is to maximize the fidelity of the robotic hand to the human hand and in certain cases even, to replace it as prosthesis for humans. This kind of dexterous robotic hand plays a crucial role as a research tool in several scientific areas, in robot services or for other challenge areas as in certain manufacturing industries.

These kinds of devices are designed with the aim of carrying out functional tasks generally realized by human beings (i.e. interacting with tools, grasping objects and so on). Because of this, the robotic hand is required to answer to some specific characteristics of a human hand: size, number of fingers, number and characteristics of the multi-joint fingers, degrees of freedom (DOFs), but an important characteristic is also the perceptive functionality (tactile perception or kinesthetic sense [13]) and the resultant movement sequencing of the fingers. The two last characteristics, both of which are part of the human cognition field, are absolutely important to understand in order to develop models of the true humanoid hand behavior. In the next paragraph, important specific terms characterizing the Humanoid Dexterous hands will be described and some examples will be given.

The degrees of freedom (or DOFs) in a robotic system, or more generally, in a linkage, correspond to a number of independent parameters that characterize the robot's motion [14],

called “configuration variables” [15]. In other words, these variables are considered as the dimension of the configuration space. For each link, different combinations of DOFs can be considered, depending entirely on the geometry of the link’s contacts. The main purpose of this thesis is to reduce the complexity of underactuated robotic hand systems through certain key design choices related to the DOFs.

Sensors play an important role, particularly for dexterous hands. Indeed, sensors have a key role in the robotic paradigms. This paradigm consists of three related steps which make the robot perform an action (move, grasp…). The three steps are: sense, plan and act. In general, they are following this order, comparable to the human brain (called hierarchical/deliberative paradigm). Sensors are placed on different parts of the robot according to the type of information desired. The physical data output from the sensors are captured and interpreted.

There exist two different types of sensors:

1- Proprioceptive sensors measuring the position, orientation and speed of humanoid’s body joints, and
2- Exteroceptive sensors, measuring the proximity of objects in relation to the robot's frame of reference.

Examples of proprioceptive sensors are given in Table 2-1:

Table 2-1: Proprioceptive sensors

Proprioceptive sensors	
Sensor	**Output measurement**
Accelerometer	Acceleration (and indirectly velocity)
Tilt	Inclination
Force	Contact force
Position	Position of the robot

Exteroceptive sensors are widely used in robotics, referring to tactile sensing. In other words, these have to do with obtaining information (torque, forces) between an object and the robot which is touching it. Exteroceptive sensors can include vision and sound sensors and can closely mimic human function.

The actuators typically refer to **"**muscles" driving the joints of the robot; these are responsible for the overall motion of the robot. They can be designed with different structures and can be electric, pneumatic, hydraulic, piezoelectric, ultrasonic, etc. There are generally two ways to mount actuators and electronics into a robotic hand:

- In the forearm: these hands are called external actuation hands (NASA/GM Robonaut Hand [16] or the Shadow Hand [3])
- In the finger body and the palm: these hands are called internal actuation hands (DLR, HIT systems [1, 2, 17]). The advantage of this type of hand is that they can be built smaller than the external actuation hand because of the decrease size of key elements as electronic components, actuators, gears and sensors which are directly integrated into the hand.

We can take as an example the DLR/HIT Hand II shown in Figure 2-1 [17]. This is a dexterous humanoid five-fingered robotic hand with multisensory capability. This hand contains fifteen DOFs (two more than the DLR Hand I): three DOFs and four joints per finger. This is an internal actuation hand because all actuators, gears and electronics for one finger are integrated in the finger's body. The whole system is articulated with super flat BLDC (Brushless Direct Current) motors allowing a better transmission.

Figure 2-1: The DLR Hand II

2.2. Underactuated Robotic hand

Recently, the underactuation concept has been introduced at Laval University [6]. An example of such systems might eventually be found in real life in spacecraft, helicopters, road vehicles or robots.

What makes underactuated robots important is that they can be classified as an alternative solution for robotic manipulation compared to humanoid dexterous hands, which, despite their versatility and stable grasping ability, are still very expensive and need to be controlled with many actuators which make the design more complex.

Underactuated hands provide not only a reduced design complexity and an enhanced flexibility of manipulation, but also they are very attractive for a wide range of applications. However, they have the drawbacks of being more task-specific, and less dexterous, compared to fully actuated hands.

Numerous examples in robotics can be considered for underactuated systems such as grasping robots [11, 12, 18, 19, 20, 21]. In underactuated mechanisms, actuators can be replaced with passive elements such as springs, limit switches or more complex compliant mechanisms [22]. These passive elements modify the adaptability of the mechanism to accommodate the grasped object. In many cases, as shown in Figure 2-2, the conventional grasping sequence implies a first position, with the finger extended, a second step where the first phalanx makes contact with the grasped object and subsequent steps in which the remaining phalanges contact the object sequentially.

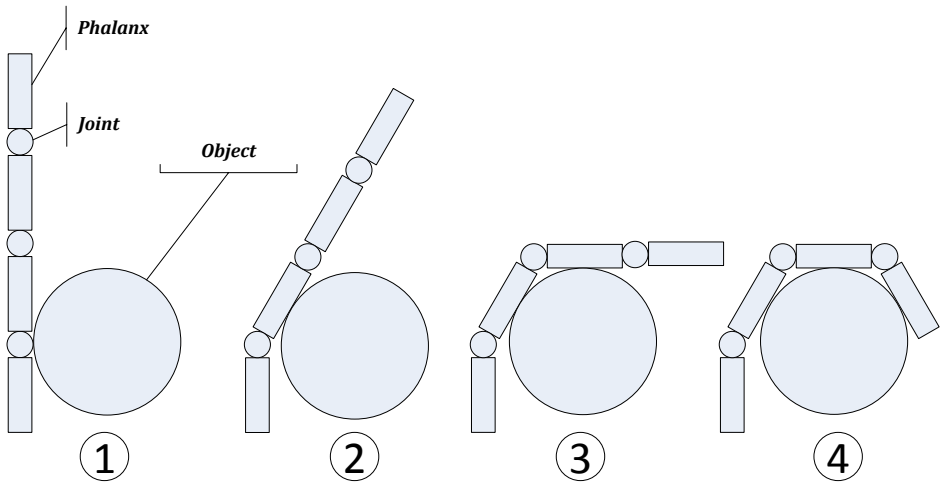

Figure 2-2: The generic grasping sequence

In any case of the corresponding Figure 2-2, for an underactactuated mechanism, the above sequence can be obtained with a continuous motion given by a single actuator.

Among the previously mentioned examples, underactuated robotic mechanisms can be activated through different means, including linkages and using tendon-driven mechanisms.

Differences between those two types of mechanisms are the grasping force needed for the application. In the case of linkages, large grasping forces are usually required. In the case of tendon-actuated mechanisms, which are our concern here, small grasping forces are needed; there tend to be friction and elasticity effects in the cables.

A tendon-actuated mechanism consists of a system using a cable, which when it is appropriately tensioned, acts in such a way as to close phalanges one by one and grasp the object (typically in an enveloping fashion). On the other hand, the linkage mechanism consists of a mechanism with multiple DOFs coupled with joints, allowing complete enveloping of the object and ensuring a stable and strong grasping. Both of the examples are illustrated in Figure 2-3:

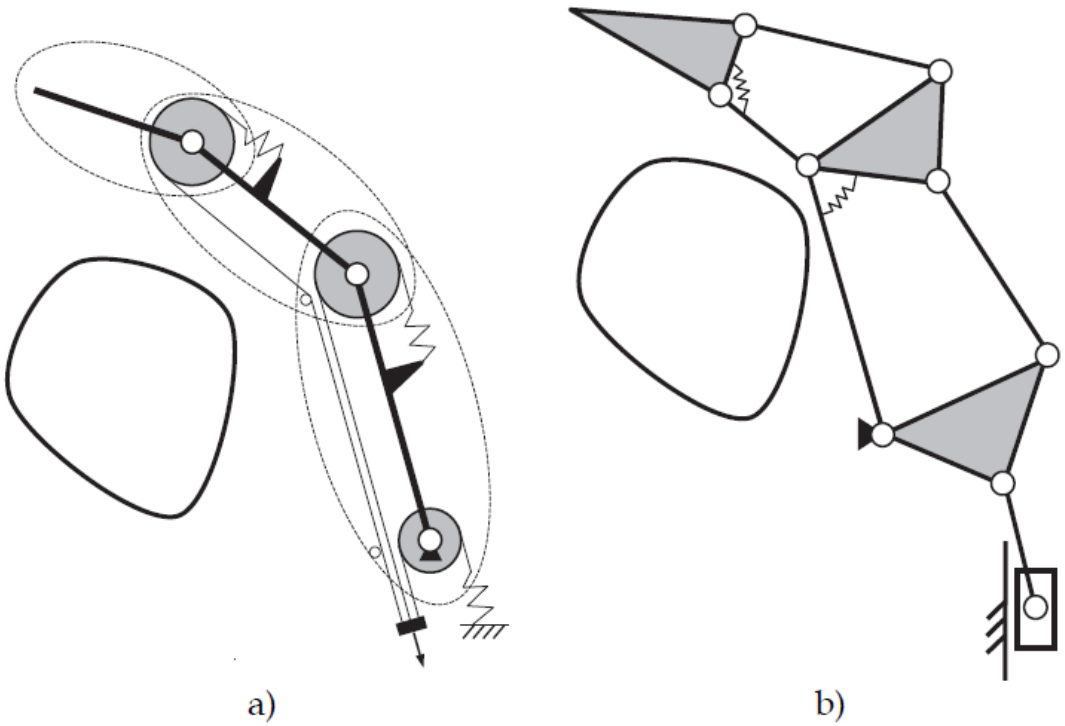

Figure 2-3: Tendon-actuated mechanism (a) and Linkage mechanism (b) [6, 23]

The commonality is that both use compliance in the underactuation strategy to ensure contact with the grasped object.

Chapter 3: Material Background

3.1. PMMA

Poly methyl methacrylate or PMMA is a thermoplastic synthetically designed from the monomer called methyl methacrylate monomer. This polymer is often used as a lightweight and shatter-resistant alternative to glass or polycarbonate (PC). Developed in 1928, this material is known under its commercial names as Plexiglas®, Altuglas®, Lucite®, Crystalite®, Perspex® or Nudec® [24].This amorphous polymer also called PMMA will be used for the phalanges of the prototype.

3.1.1. Synthesis

The synthesis of PMMA occurs with the help of radicals which start the polymerization chain reaction. For this polymerization, the anionic polymerization is also possible.

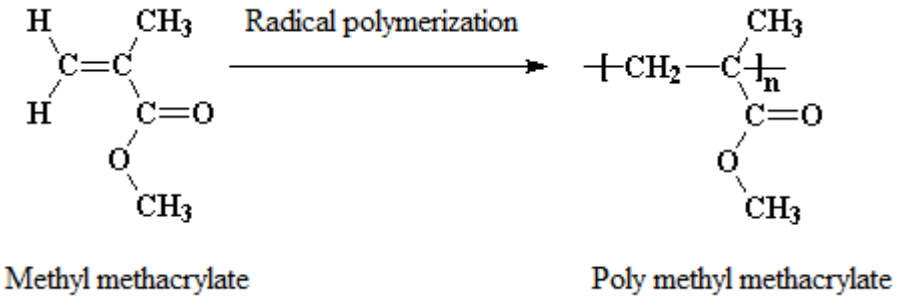

Figure 3-1: Polymerization of the PMMA

The polymerization chain reaction, also called radical polymerization, involves free radicals. The process occurs in three steps:

1- Initiation

2- Propagation

3- Termination

During the initiation step, an active center (primary radical) is created on which the polymer chain will expand. This generation is possible thanks to a radical initiator. Producing primary radicals is possible through different initiators:

- Thermic initiators using thermal decomposition (i.e., azobisisobutyronitrile or AIBN)
- Photochemical initiators using light or UV radiation (benzile)
- Redox reaction initiators

During the second step, propagation, the polymeric chains keep increasing in length by successive additions of monomer units on the growing radicals. The repetition of the propagation reaction governs the degree of polymerization of the polymer and thus the number-average molecular weight.

Then the chain termination occurs unless the reaction is completely free of contaminants. In this case, the polymerization is considered to be “living” because propagation can continue if more monomer is added. Termination processes can occur differently:

- By combination of 2 active chains
- Combination of an active chain and an initiator radical (oxygen)
- Interaction with impurities or inhibitors

3.1.2. General Properties

This linear and amorphous polymer is mainly valued for several properties:

- Rigidity (E= 2.5 GPa)
- Optical properties comparable to crystals (92% in transmission)
- Weather resistance

Nevertheless, physical and chemical characteristics can vary sensitively, according to the importance of the molar mass, the rate of the free monomers in the polymer and the quantity of adjuvants, notably plasticizer. The material processes can also have an influence.

Table 3-1 shows the important properties of PMMA:

Table 3-1: General properties of PMMA

Properties	Characteristic value
Physical Properties	
Refractive index	1.493
Mechanical Properties	
Ultimate tensile strength	65 to 75 MPa
Yield strength	30 MPa
Ultimate flexural and compressive strength	110 MPa
Ultimate shear strength	70 to 80 MPa
Thermal Properties	
Glass transition range (commercial grades)[1]	85-160°C

[1] The range of temperature increase because of the vast number of commercial compositions we can find (additives can be added in order to increases PMMA's properties). Therefore, the average glass transition is 105°C

3.1.3. Applications

Major applications of PMMA include:

- Automotive industry - rear lamps, light fixtures
- PMMA sheet - bathtubs
- Glazing – signs
- Composites - sinks, basins and bathroom fixtures
- Contact lenses, bone cements
- Membrane for dialysis
- Dental restorations
- Road lines

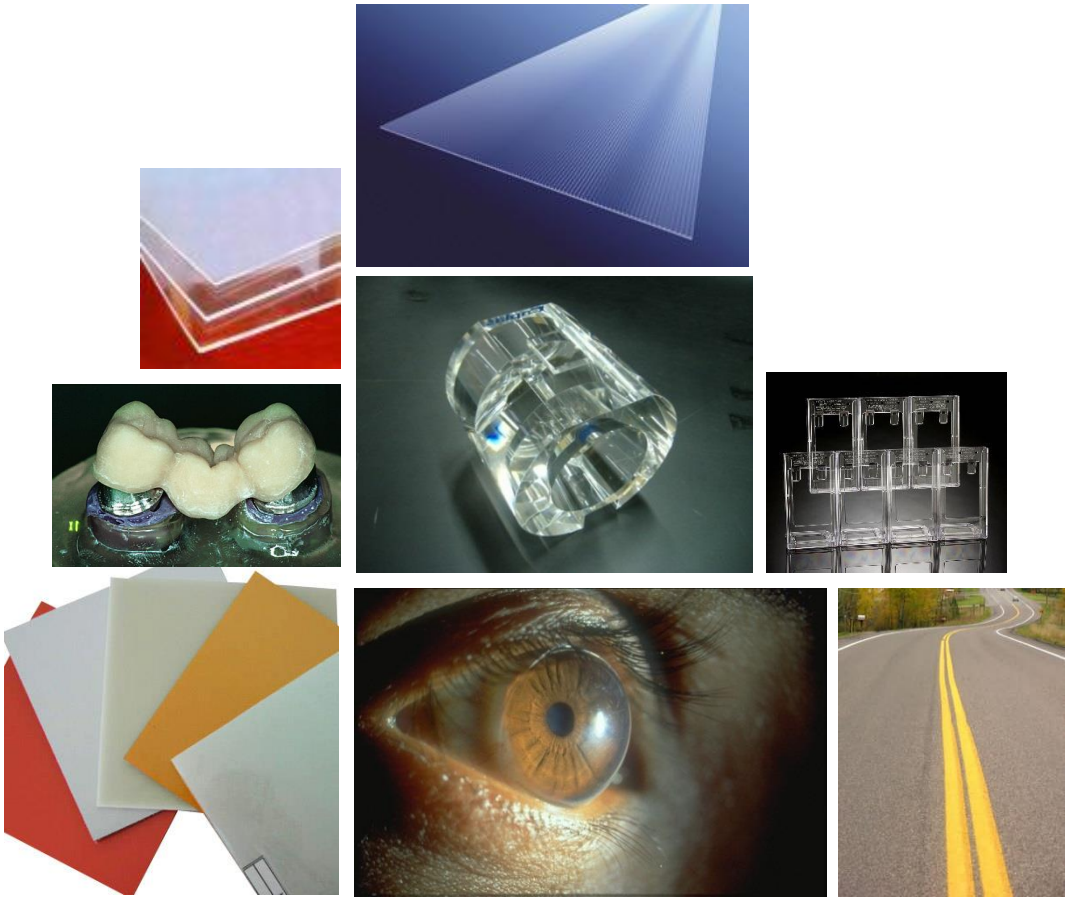

Figure 3-2: Applications for PMMA

3.2. Nitinol

3.2.1. Introduction

Because of their special characteristics, titanium alloys are widely used in aerospace, naval, medical and chemical engineering. Among these classes of alloys we can find NiTi alloys, called shape memory alloys (SMA). These NiTi alloys were discovered in 1963. At the origin of its discovery, the U.S Naval Ordnance Laboratory (NOL) gave the name Nitinol (Nickel Titanium Naval Ordnance Laboratory), for this new type of alloy [25]. Since this discovery, scientific interest kept growing and many other alloys have been acknowledged to be SMA (the most popular being those containing copper, Cu-Al-Ni and Cu-Al-Zn). As for titanium and its alloys, the market share of SMA increased more and more in the field of biomaterials since 1962 as shown in Figure 3-3, especially in orthodontic, orthopedic, vascular and neurosurgical fields [26, 27].

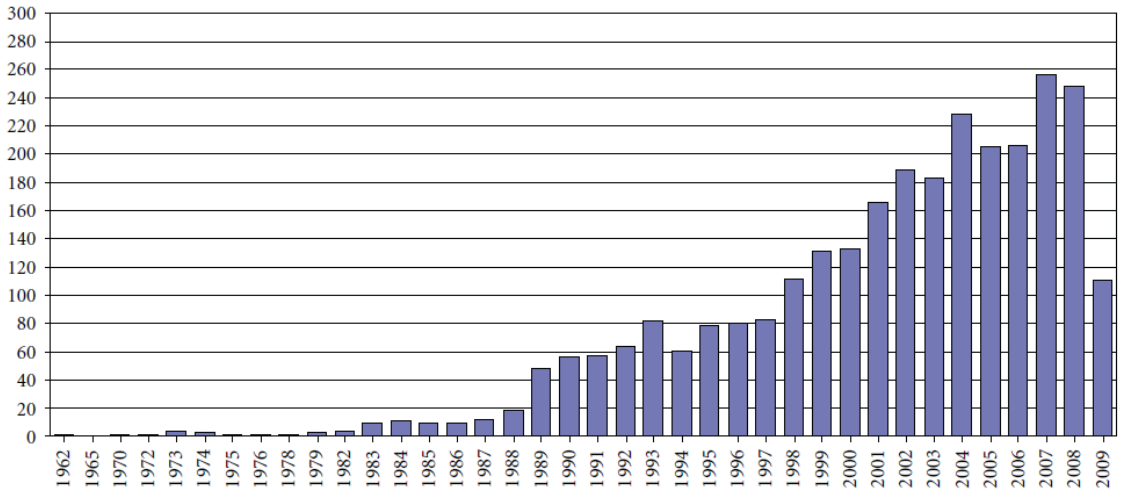

Figure 3-3: Number of publications per year

3.2.2. Characteristic phases of the Nitinol

NiTi alloys are characterized by two different temperature-dependent phases: the austenite phase (A), stable at high temperatures ($T>A_f$: the austenite finish transformation

temperature) and the martensitic phases (M), stable at low temperatures ($T<M_f$: the martensitic finish transformation temperature) [26]. Both phases also have distinct structures, accompanied by distinct properties. Respectively, austenitic and martensitic phases are body centered cubic (BCB) and rhombus structured as shown in Figure 3-4.

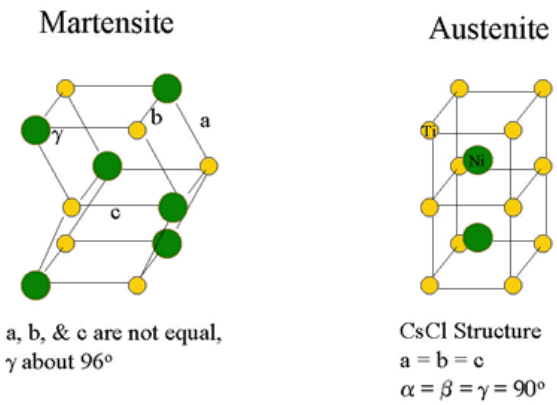

Figure 3-4: Martensitic and austenitic structures

3.2.3. The thermoelastic martensitic transformation (TMT)

The transformation between the austenite and the martensite depending on the temperature is called thermoelastic martensitic transformation (TMT) [28]. TMT, which give the alloy its interesting properties, arises because the crystal lattice structure needs to receive the minimum energy for a given temperature. This transformation, and the reverse transformation, is a shear-dominant diffussionless solid-state phase transformation occurring by nucleation and growth of the martensitic phase from the parent austenitic phase. Austenitic phase is called parent due to the symmetry of its structure, compared to the martensitic phase. The transformation between austenite and martensitic can be obtained either by:

- Changing the temperature: from austenite to martensite by decreasing the temperature (thermally induced martensite) and increasing the temperature from martensite to austenite
- Mechanical stress: from austenite to martensite by applying pure mechanical stress (stress induced martensite) and removing it from martensite to austenite.

The simple changing of the temperature to obtain martensite from austenite is called "twinning", corresponding to mirror symmetry of the displacement of the atoms across a particular atom plane, the twinning plane [29].Then, by applying mechanical stress to it, the martensitic structure can be easily deformed. This step is called "detwinning" [29]. This phenomenon, responsible for the shape memory behavior, which will be explained in later section, can be illustrated in Figure 3-5.

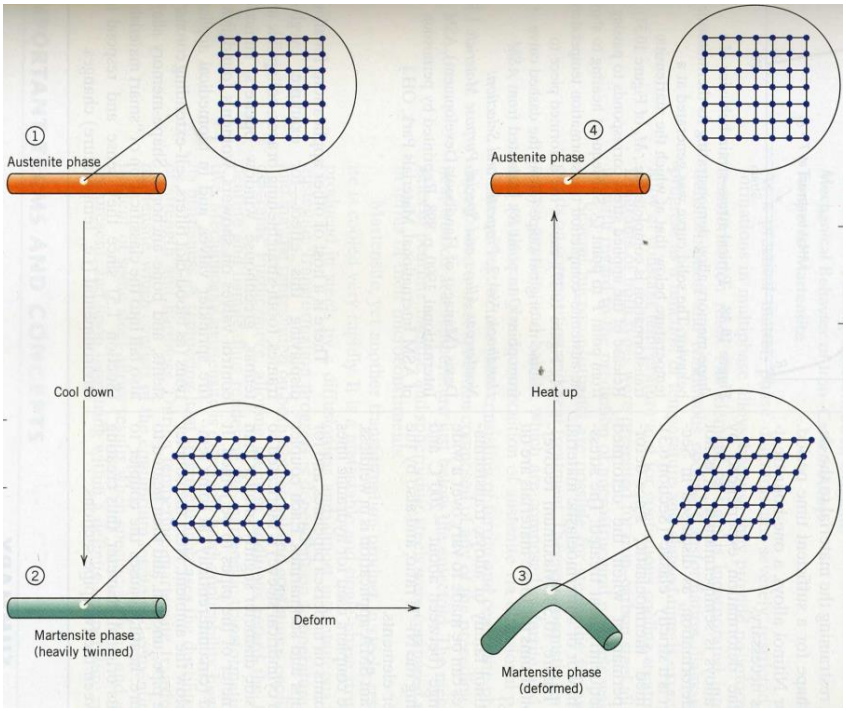

Figure 3-5: Twinned and detwinned process

After this "detwinning"step, once the martensite phase is heated to a temperature above A_f, the Nitinol can easily retrieve its original shape, with no trace of the previous steps.

As we previously saw, the transformation between austenite and martensite is characterized by different temperatures. These temperatures can be identified by differential scanning calorimetry (DSC). The specific temperatures from martensitic to austenitic phase occur upon heating and the specific temperatures from austenitic to martensitic phase occur upon cooling. The difference between these two cycles is called hysteresis. Figure 3-6 shows a DSC thermogram of a NiTi alloy and the characteristic temperatures. The hysteresis corresponds to the temperature difference when the material is 50% transformed to austenite (upon heating) and 50% transformed to martensite (upon cooling). This is this hysteresis which gives these alloys, their desirable mechanical properties.

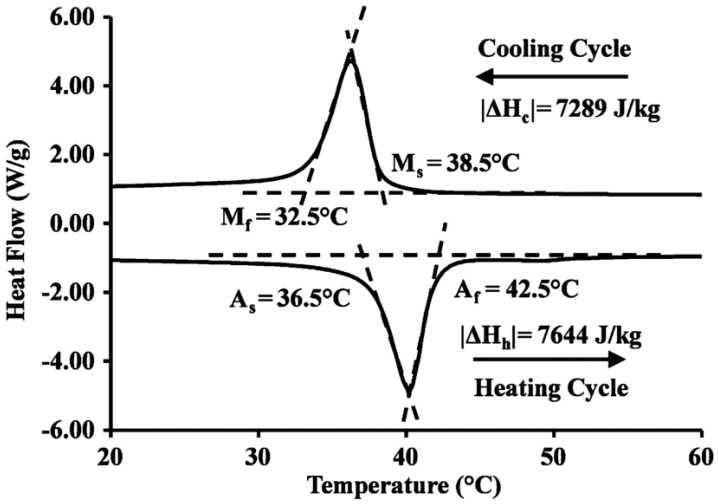

Figure 3-6: DSC Thermogram of a NiTi alloy

3.2.4. Mechanical and functional properties of NiTi alloys

Mechanical properties of NiTi alloys are different and sometimes better than other typical alloys. Depending on the thermomechanical cycles or the loading cycles to which NiTi alloys are subjected, or the composition, mechanical properties can change. An overview of the basic mechanical properties comparing the different phases of the NiTi alloy (austenite and martensite) is shown in Table 3-2.

Table 3-2: Table of mechanical properties of Nitinol [30]

	Martensite	Austenite
Young's modulus	28-41 GPa	75-83 GPa
Ultimate Tensile Strength (fully annealed/work hardened)	895/1900 MPa	895/1900 Mpa
Poisson ratio	0.33	0.33
Elongation at failure (fully annealed/work hardened)	25-50%/5-10%	25-50%/5-10%
Recoverable strain	8-10%	8-10%

3.2.5. One-way shape memory effect (OWSME)

Typically, the shape memory effect is obtained when the alloy in martensitic form is plastically deformed below the characteristic temperature of the martensitic phase (M_f). Once it is heated above the characteristic temperature of the austenite phase (A_f), then the alloy can recover its original shape corresponding to the austenitic parent phase. The shape memory effect is schematized in Figure 3-7. The shape memory effect is possible thanks to a high mobility at the interface of the material, in particular during the cooling from step (C) to step (A). This shape memory effect is called one-way shape memory effect (OWSME) because shape is recovered only during the heating portion.

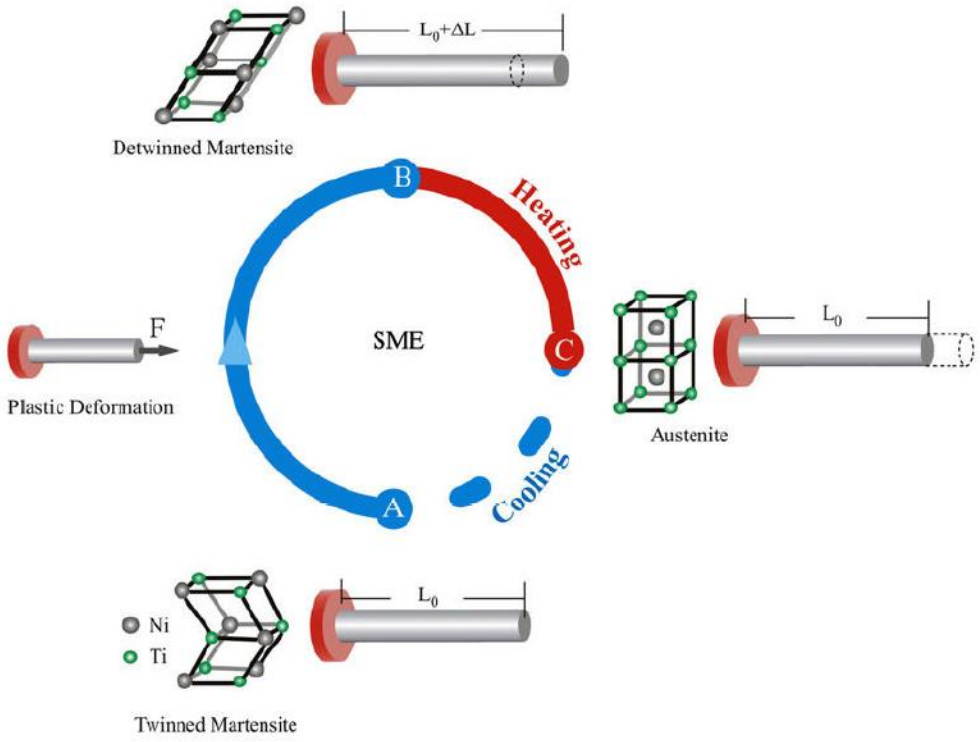

Figure 3-7: The shape memory effect showing the original alloy (A) plastically deformed (B) and recovering its original shape after heating (C) [28]

The shape memory behavior depends on different factors: the proportion of Ni or other alloying elements as well as the thermo-mechanical treatment and the aging of these alloys. Changing these parameters will affect the structure and therefore the shape memory behavior [31].

3.2.6. Superelasticity or pseudoelasticity

One of the important properties of the Nitinol is the superelasticity or pseudo-elasticity. This characteristic, observed for the first time in 1932 by Ölander [31], means that the alloy is capable of being deformed reversibly under the effect of a stress.

For the record, for classic alloys and plastics, the elasticity is the ability of a material to return to its original shape after deformation when the stress (or applied force) is released. The characteristic stress-strain curve for a classic alloy is shown in Figure 3-8.

Important characteristics from this curve can be obtained:

- Elastic limit: beyond this point, permanent deformation will occur. This limit gives one maximum strength value called yield strength (in MPa) corresponding to the limit of deformation (in %).
- The young's modulus corresponding to the slope of the linear elastic part of the stress-strain curve, defined by the following formula: $E = \frac{\sigma}{\varepsilon}$
- The fracture point: the maximum stress that a material can withstand while being mechanically deformed (tensile stress, compressive stress…) before breaking.

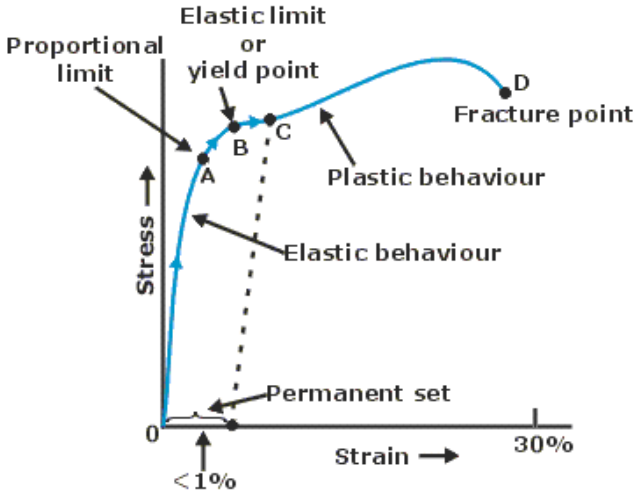

Figure 3-8: A typical stress-strain curve for a ductile metal [32]

In comparison, typical stress-strain curves for SMAs are different. The first part of the curve is the same as the one for a conventional material. However, it then presents a plateau of deformation, still corresponding to the elastic area, therefore reversible. This means that if, along the entire plateau, the previous load is released, and then the material recovers its initial shape for deformation up to 8%, which is 10 times higher than the best steels. Figure 3-9 compares both superelastic Nitinol and stainless steel elastic strain range.

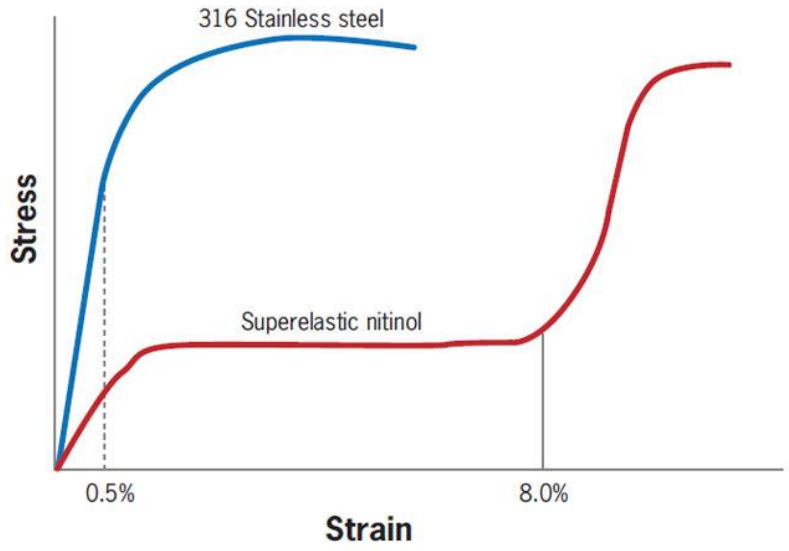

Figure 3-9: The elastic strain range for superelastic Nitinol compared to stainless steel

The phenomenon of superelasticity, is associated with the stress induced reversible transformation from austenite to martensite (and reversibly), occurring above A_f. When a stress is applied, austenite is transformed into detwinned martensite, unstable at high temperature. Thus, by unloading, martensite transforms back to austenite and Nitinol can fully recover its original shape. Due to the hysteresis cycle, paths upon loading and unloading are different, meaning that stress plateau will be on different levels. This difference in loading and unloading paths comes from the energy dissipation during the transformation. The energy during the transformation from austenite to martensite is less significative than from martensite to austenite (because of the instability of the martensite at high temperatures). Figure 3-10 shows the stress-strain curve upon loading and unloading the Nitinol.

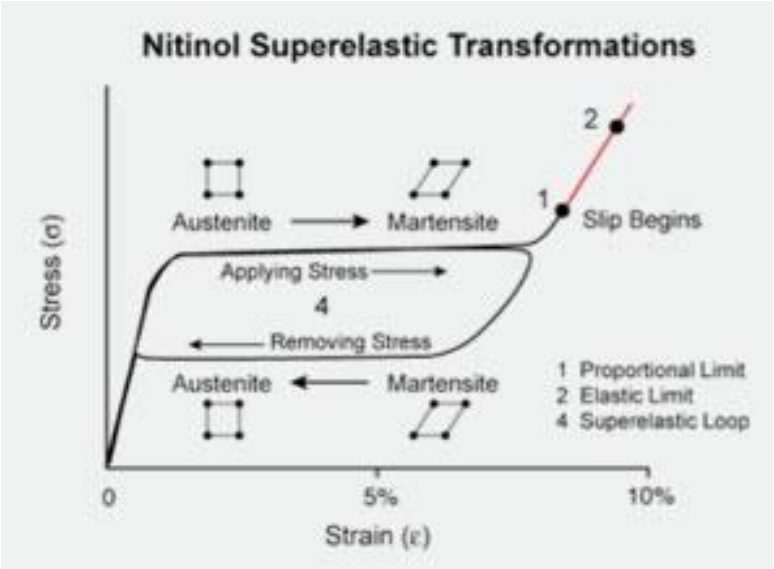

Figure 3-10: Nitinol superelastic transformation [33]

3.2.7. Two-way shape memory effect (TWSME):

The TWSME is similar to the OWSME but this effect causes a modification of two different desired shapes only by changing the temperature across A_f and M_f [31]. In Figure 3-11 (right-hand side), when large stress is applied on the specimen (a), irreversible deformations can occur (b) and the specimen cannot return back to its original shape (c). Stability of the shape is a compromise because of the high deteriorations during the working cycle. So by applying heat the specimen will return back to a shape other than the original one (c) and using cooling and heating cycles, the specimen will change its shape between (c) and (d).

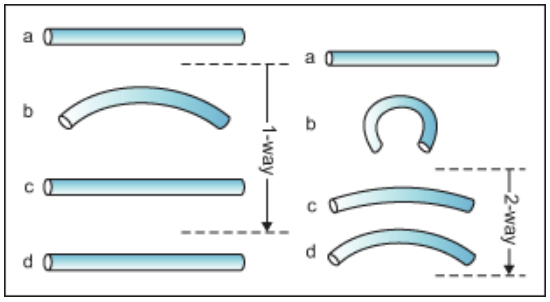

Figure 3-11: Difference between one (left) and two (right) - way shape memory effect

3.2.8. Manufacturing process of Nitinol

The manufacturing process consists of several steps: melting and casting, forging and hot rolling, cold drawing, forming and finally shape memory treatment [31]. The process starts with the melting of the alloy using a vacuum arc (VAR) technique [34] allowing a better uniform distribution of transformation temperature along the ingot. The transformation of the ingots then follows, using a hot forging method, into rolled bars and coils. Resulting products need to be subsequently drawn to obtain finished sizes. Before obtaining the commercial shape desired by companies, Nitinol has to be cold worked when coming off the drawing machine (as-drawn wire) and then fixtured and constrained in the desired form and then heat treated (for example, superelastic materials need to be heat-treated at about 500°C) to obtain desired functional properties. The heat treatment depends on the time, the technique, the equipment used as well as the physical characteristics of the product. Modifications to the heat treatment methods or the temperature of heat treatment influence the material transformation temperatures and properties of the shape memory alloys.

Chapter 4: Physical design & Assembly

4.1. Design Concept

In the proposed underactuated finger, the grasping sequence is slightly different compared to the traditional approach shown in Figure 2-2. The finger is designed to have an initial closed position. This is achieved through shape-memory (Nitinol) members which function both as springs and as the compliant finger joints themselves, while giving the finger its initially closed shape.

The advantages of such an initial close position design are that:

- We don't have to be in contact with the object to actuate the closure of the phalanges
- It produces a simple and more natural movement
- A passive closure is performed implying that the balancing force counteracting the applied external force is produced by the grasped object itself
- Objects can be grasped without using too much energy

A tendon connected to a single actuator is routed along the back of the finger through an offset channel to generate the necessary moment at the joints. To grasp an object, the tendon is displaced to open the finger, and after moving the hand into position, releasing tension in the tendon allows the finger to close around the object. This sequence can be observed in Figure 4-1, where the tendon tensile force is denoted as F. A uniform rate of closure of all the phalanges is targeted through careful design of the individual joint stiffnesses (in contrast to the phalanx-by-phalanx sequence shown in Figure 2-2). This permits pinch grasps as well as enveloping grasps depending on the position of the hand relative to the grasped object. Our configuration also allows modulation of grip by tension in the actuation cable. Only the maximum force is limited by the design.

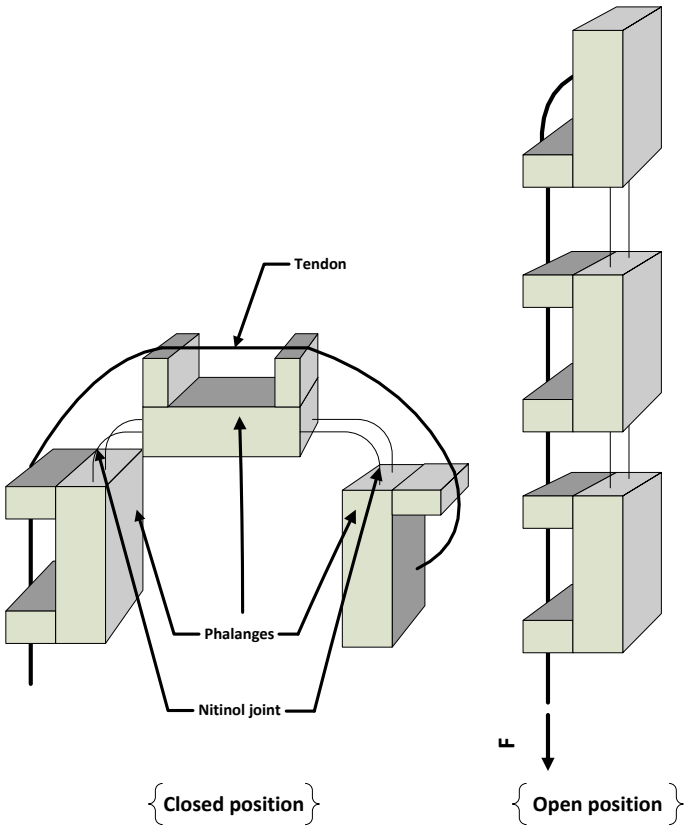

Figure 4-1: Schematic diagram for closed (left) and open (right) positions

4.2. Materials used

4.2.1. PMMA

For prototyping the underactuated finger, PMMA (Mc Master-Carr, Elmhurst, IL) was used for the phalanges. PMMA was mainly chosen for ease of manufacture. But the high transparency of this material allows observation of defects and cracks during the machining of the pieces and the introduction of the Nitinol joints. In a more commercial final version of this design, a tougher material like aluminum may be used.

Three pieces of PMMA, used as phalanges, were cut using the Epilog Mini 18 laser (30-W laser fabrication system) with CorelDraw as the user interface and the settings specified in Appendix D. The rectangular pieces have dimensions of 25.4 x 19.1 x 6.4 mm (1 x $\frac{3}{4}$ x $\frac{1}{4}$ in). Holes were drilled in the ends to a depth of 10 mm (0.4 in) to receive the Nitinol joints. Also,

rectangular pieces with dimensions of 19.1 x 6.4 x 12.7 mm ($\frac{3}{4}$ x $\frac{1}{4}$ x $\frac{1}{2}$ in) were cut to make the offset channel which will generate the moment.

Figure 4-2: Epilog Mini 18 laser

4.2.2. Nitinol

Nitinol (Memry, Bethel, CT) was used for the compliant joints. The two features of Nitinol which make it suitable for this application are its superelasticity at room temperature (A_f = -15 ± 10 °C) and the ability to imbue the material with preferred shape through heat treatment. The chosen wire diameters for the first and second prototypes were 1.30 and 0.89 mm (0.051 in and 0.035 in) respectively. Young's modulus for the Nitinol is 20.6 ± 2.8 GPa (determined in a later section). The length of wire in each joint is determined as follows.

4.2.3. Tendon Actuator

Finally, a 1.59-mm (1/16-in) diameter tendon made of Nylon-coated galvanized steel rope was used to open the finger.

4.3. Dimensional Synthesis and Prototyping

4.3.1. Dimensional Synthesis

The process of specifying dimensions for the Nitinol wires and manufacturing the components was carried out in several stages:

- Finding the theoretic tip force and the corresponding torques carried in the Nitinol joints
- Calculating the desired length of the Nitinol wire using the angular deflection formula for large deformation based on the selected cross section
- Designing and manufacturing a form used for bending the Nitinol to the correct shape
- Heat-treating the Nitinol

The Shadow dexterous hand [3] was used as a benchmark for specifying the target grasping force. In Table 4-1, the measured maximum force and the maximum torque for two types of joint are listed. The two types of joints concerned are:

- MCP joint or metacarpophalangeal joint
- PIP joint or proximal interphalangeal joint

The two corresponding joints are shown and circled in Figure 4-3.

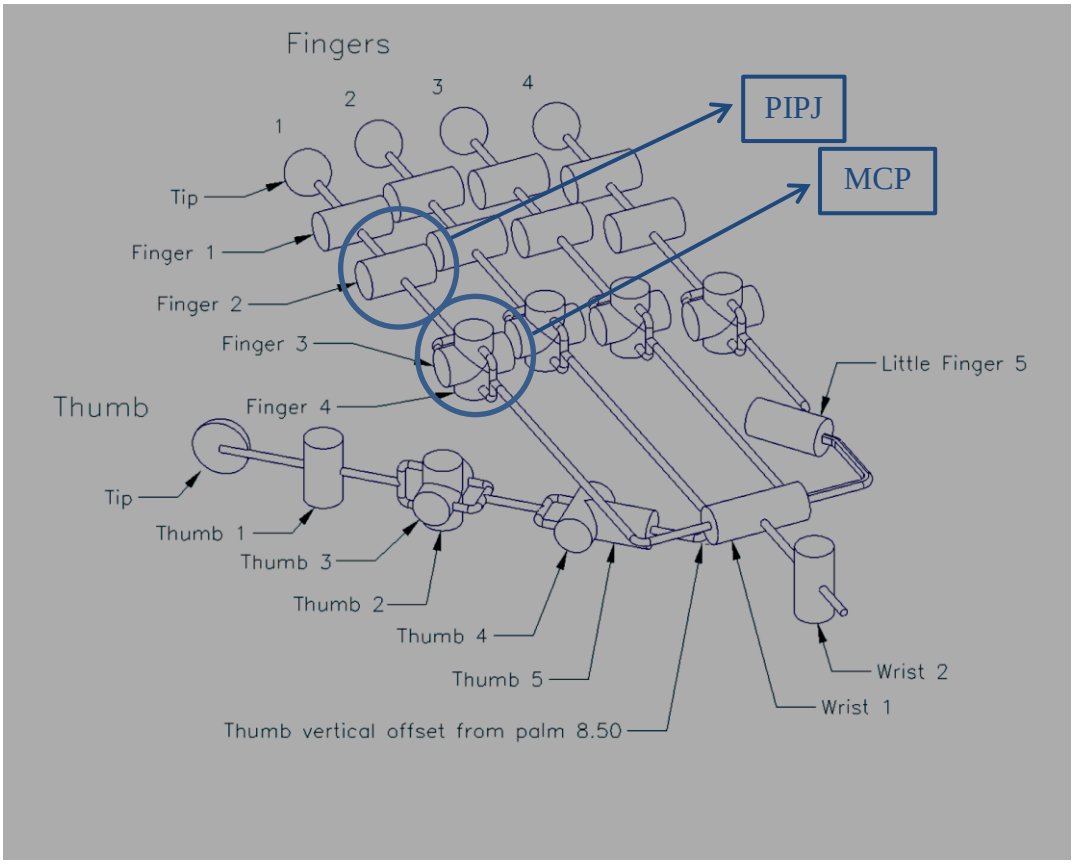

Figure 4-3: Kinematic diagram of the finger joints of the Shadow dexterous hand

Table 4-1: Target values of maximal available force / torque

Shadow Dexterous Hand [3]		
Joint	Maximum Force (N)	Maximum Torque (N.m)
MCPJ	2.9	0.27
PIPJ	9.4	0.46

Maximum torque is obtained by multiplying the force by the distance between each joint and the fingertip. Figure 4-4 shows the precise length of the finger and the corresponding distance from the fingertip to the different joints (51 and 96 mm) of the finger.

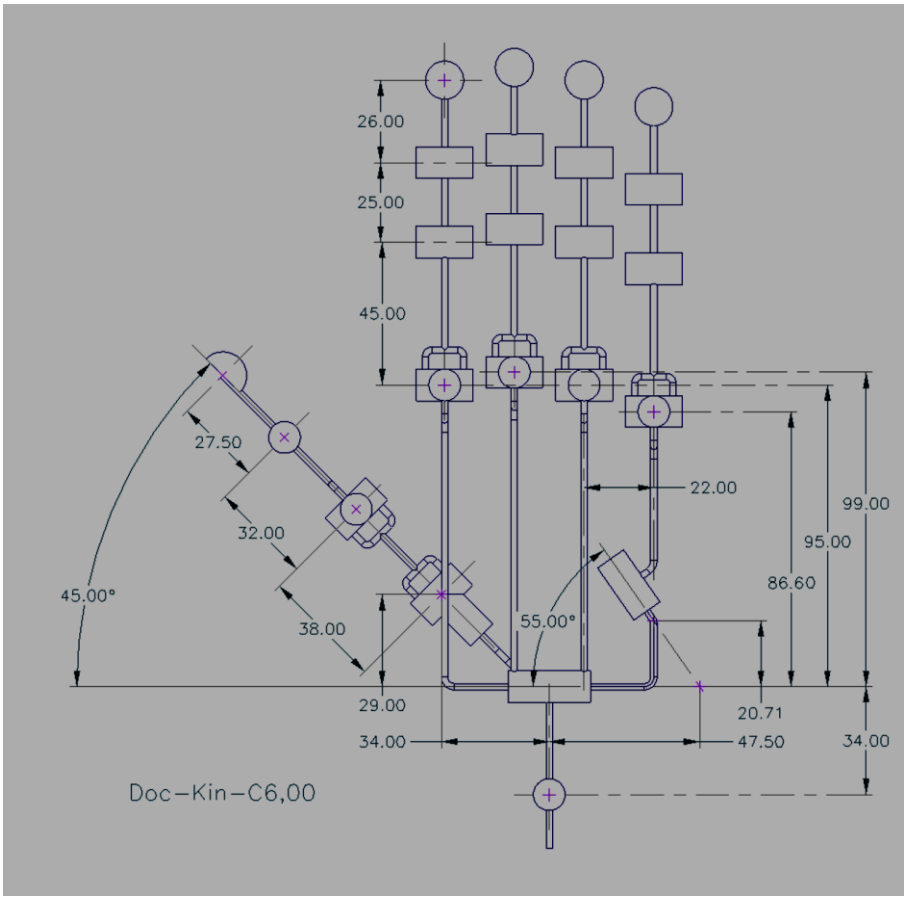

Figure 4-4: Kinematic diagram of the first finger length of the Shadow Dexterous Hand

For our prototype, instead of different forces applied on the joints, as specified for this example, we'll consider a unique fingertip force, which will give us the conservative moment of the joint according to the length of the finger. Potential fingertip forces of 10 N and 3 N were used as a guideline to find a reasonable length of Nitinol wire, corresponding respectively to the target torque applied on the PIPJ and MCPJ. The kinematic diagram for the desired prototype is shown in Figure 4-5.

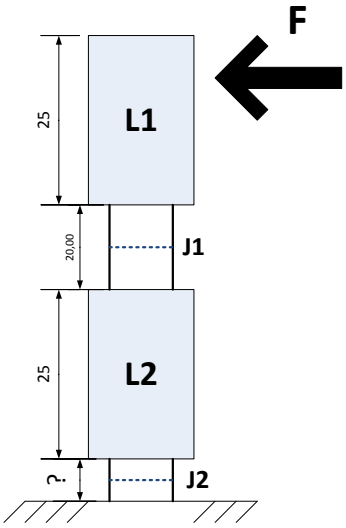

Figure 4-5: Kinematic diagram for the prototype

The deflected angle of a compliant beam is given as [22]:

$$\theta_0 = \frac{M_0.L}{E.I} \quad (1)$$

with:

- θ_0 the deflected angle of the beam end
- M_0 the moment applied to the beam
- L the length of the beam
- E the stiffness of the beam material
- I the second moment of area of the beam cross section

The cross section moment of inertia for a round wire is:

$$I = \frac{\pi.D^4}{64} \quad (2)$$

with D being the diameter of the section (here we use D = 1.3mm since this is commercially available). We can now substitute the expression for the moment of inertia I (2) into the deflected angle formula (1), which gives:

$$\theta_0 = \frac{M_0.L}{E.\left(\frac{\pi.D^4}{64}\right)} \quad (3)$$

or,

$$\theta_0 = \frac{64.M_0.L}{E.\pi.D^4} \quad (3)$$

If the diameter is first specified, and the load in the compliant member corresponds to the fingertip forces previously assumed to be either 3 or 10 N, the necessary active length of Nitinol wire can be approximately found:

$$L = \frac{\theta_0.E.\pi.D^4}{64.M_0}$$

To design a finger which is initially closed, we choose a resting angle of 90°, or in other words an available joint torque which decreases linearly from its maximum when the finger is straightened, down to zero when the finger joints are curled in at 90°. The active joint length formula then becomes:

$$L = \frac{E.\pi^2.D^4}{128.M_0} \quad (4)$$

In this case, the moment applied at the free end of the joint M_0 corresponds to the tip force multiplied by the length of the first phalanx (L_1):

$$M_0 = F.L_1 \quad (5)$$

The expression of the length (4) of the first joint (J_1) is now:

$$J_1 = \frac{E.\pi^2.D^4}{128.F.L_1}$$

The value of J_1 for a tip force of 3 N is:

$$J_1 = \frac{(24.9 \times 10^9) \times \pi^2 \times (1.3 \times 10^{-3})^4}{128 \times 3 \times 0.025}$$

$$J_1 = 73\ mm$$

The value of J_1 for a tip force of 10 N is:

$$J_1 = \frac{(24.9 \times 10^9) \times \pi^2 \times (1.3 \times 10^{-3})^4}{128 \times 10 \times 0.025}$$

$$J_1 = 22\ mm$$

For a value of 10 N, a joint length of 22 mm is obtained. The other value of 73 mm could not be used as joint length because it is too large. The force of 10 N has also been chosen because it corresponds to the stiffer joint of the shadow dexterous hand and it gives a reasonable length.

In this configuration, the moment applied on joint 1 (M_1) and the moment applied on joint 2 (M_2) can be determined using two equations:

$$M_1 = F.\left[L_1 + \left(\frac{J_1}{2}\right)\right] \quad (6)$$

$$M_2 = F.\left[L_1 + J_1 + L_2 + \left(\frac{J_2}{2}\right)\right] \quad (7)$$

with a chosen value of: $J_1 = 22$ mm, M_1 is calculated using (6):

$$M_1 = 10\left[25 + \left(\frac{22}{2}\right)\right]$$

$$\boxed{M_1 = 360\ N.mm = 0.36\ N.m}$$

If we initially neglect the effect of the sizes of the joints (J_1 and J_2) on the moments, based on the lengths of the links (L_1 and L_2) being equal, we can assume the moment in joint 2 will be double that in joint 1. Therefore, we can consider the ratio: $M_2 = \left(\frac{77.5}{36}\right).M_1(8)$ based on the geometry of Figure 4-5.

$$M_2 = F.\left[L_1 + J_1 + L_2 + \left(\frac{J_2}{2}\right)\right]$$

Using (7) and (8), we can write:

$$M_2 = F.\left[L_1 + J_1 + L_2 + \left(\frac{J_2}{2}\right)\right] = \left(\frac{77.5}{36}\right).M_1$$

We can solve for J_2:

$$10.\left[25 + 22 + 25 + \left(\frac{J_2}{2}\right)\right] = \left(\frac{77.5}{36}\right).M_1$$

$$10.\left[25 + 22 + 25 + \left(\frac{J_2}{2}\right)\right] = \left(\frac{77.5}{36}\right).360$$

$$\left[72 + \left(\frac{J_2}{2}\right)\right] = \left(\frac{77.5}{36}\right).36$$

$$\left[72 + \left(\frac{J_2}{2}\right)\right] = 77.5$$

$$\boxed{J_2 = 11\ mm}$$

Note that because of the equality of L_1 and L_2, no iteration is necessary to solve for J_2 (i.e., the assumed value implied by the use of the ratio 77.5/36 matches with the calculated value. Then we can calculate M_2:

$$M_2 = 10.\left[L_1 + J_1 + L_2 + \left(\frac{J_2}{2}\right)\right]$$

$$M_2 = 10.\left[25 + 22 + 25 + \left(\frac{11}{2}\right)\right]$$

$$\boxed{M_2 = 775\ N.mm = 0.78\ N.m}$$

To summarize we have:

Table 4-2: Sum up of the calculated length and the related torques

Joint	Length (mm)	Maximal torque carried by the joint's pair (N.m)
PIPJ (Joint 1)	22	0.36
MCPJ (Joint 2)	11	0.78

The next task consisted to design a form that will allow heat treatment of the Nitinol while achieving a 90° bend in the wire. Since the length of the wire is known from the previous formula, the radius of curvature can be calculated. The length corresponding to a 90° bend follows a quarter circle with an active length of:

$$L = \frac{2\pi r_c}{4} \quad (9)$$

The radius of curvature is then:

$$r_c = \frac{2L}{\pi}$$

With the desired shape now determined, a form can be fabricated to heat treat the Nitinol wire. We used a metal plate receiving a large shoulder screw with the head size matching the desired radius of curvature and several small pins or screws to maintain contact with the form, as shown in Figure 4-6. The Nitinol on the plate is placed such as to bend the active length, and the straight ends are necessary to assemble the PMMA and the Nitinol together.

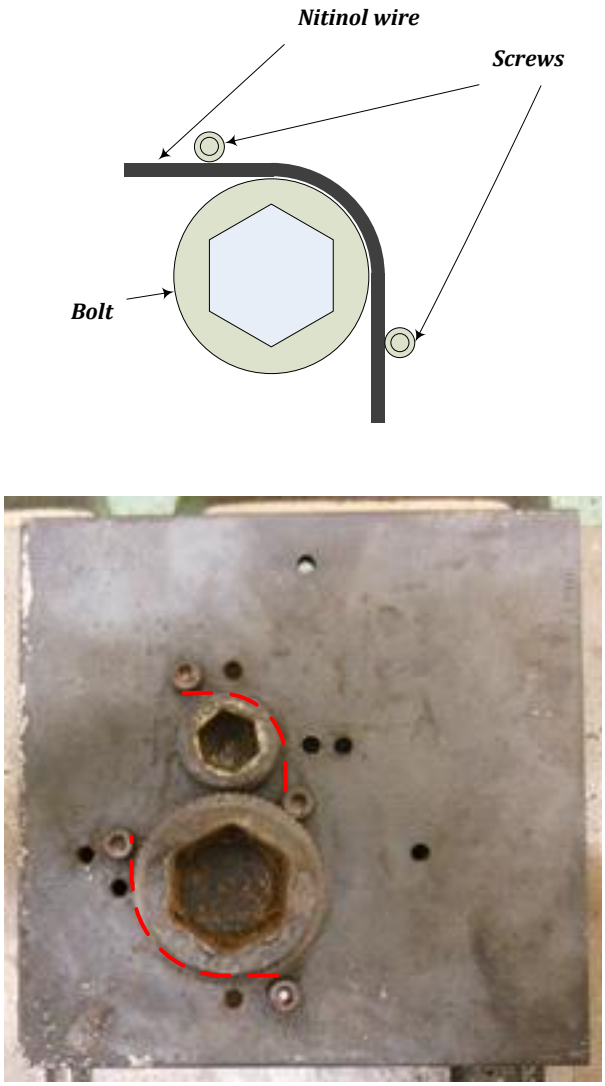

Figure 4-6: Bending form for the Nitinol wire

Four lengths of Nitinol wire were cut (2 for the MCPJ and 2 for the PIPJ), secured on the plate and finally heat treated to obtain the desired curvature. The heat treatment for each sample of Nitinol was 10 minutes at 600°C.

4.3.2. Prototyping

For the first prototype, the length and radius of curvature corresponding to each joint has been calculated using the previous formulas with:

- E = 24.9 GPa – Young's modulus of the Nitinol wire
- D = 1.3 mm – diameter of the Nitinol wire
- $\theta_0 = \frac{\pi}{2}$ – deflection angle of the beam

The resulting values for the selected wire cross section should ideally be the ones summarized in Table 4-3.

Table 4-3: Length and radius of curvature for finger joints

Joint	Torque (N.m)	Active length of Nitinol (mm)	Curvature radius (mm)
Joint 2	0.78	11	7
Joint 1	0.36	22	14

The eventual prototype was fabricated with values approximating the ideal values:

Table 4-4: Values of the prototype approximating the ideal values

Joint	Torque (N.m)	Active length of Nitinol (mm)	Curvature radius (mm)
Joint 2	0.46	12	7.48
Joint 1	0.27	20	12.75

With the dimensions determined and the Nitinol cut and formed, the Nitinol wire and the PMMA phalanges can be pieced together to create the prototype shown in Figure 4-7 and 4-8. Notice that pairs of wires are used for each joint. This is to stiffen the finger against bending and torsion in off-axis directions while allowing the desired (natural) finger motion. (Of course this increases the supported joint moments.)

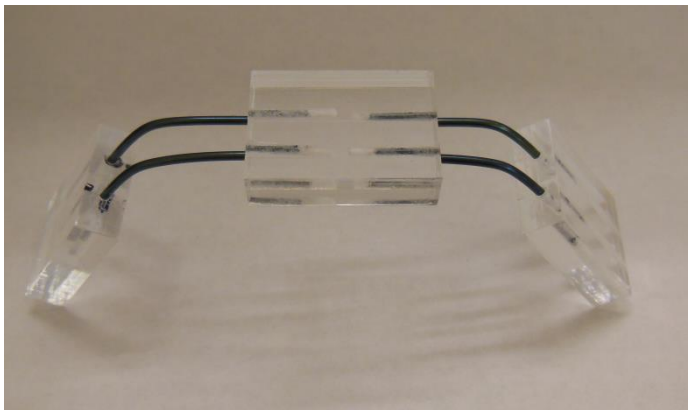

Figure 4-7: First prototype of the underactuated finger

Figure 4-8: The prototype shown in a partial grasp position

This first prototype did not completely attain the goal. Modifications needed to be performed to make a functional prototype. Indeed, the finger joints of the prototype are supposed to be bent at 90° in a complete grasping position, which is not the case as shown in Figure 4-8. This first difference is due to a manufacturing imperfection of the plate, which was corrected in the second prototype. Also, in this prototype, the stiffness of the joints was too high, ultimately limiting the articulation of the finger by the tendon. With this in mind, a second more fully functional prototype has been designed and built based on lessons learned from the first prototype.

The length and radius of curvature corresponding to each joint remain the same as the first prototype, but the diameter of the wire is changed to 0.89 mm. Now, rearranging the previously presented formulas (3), the joint torque is calculated as:

$$M_0 = \frac{\theta_0 . E . \pi . D^4}{64 . L}$$

$$M_0 = \frac{E . \pi^2 . D^4}{128 . L}$$

The torque values for the selected wire cross section are presented in Table 4-5:

Table 4-5: Calculated torque corresponding to wire diameter

Joint	Active length of Nitinol (mm)	Curvature radius (mm)	Diameter (mm)	Torque (N.m)
Joint 2	11	7	0.89	0.11
Joint 1	22	14	0.89	0.06

Since joints are doubled for the joint 1 and 2, we obtain:

Table 4-6: Calculated torques corresponding to the doubling of the wires

Joint	Active length of Nitinol (mm)	Curvature radius (mm)	Diameter (mm)	Torque (N.m)
Joint 2	11	7	0.89	0.22
Joint 1	22	14	0.89	0.12

The second fabricated prototype approached these parameters as follows:

Table 4-7: Values of the torque recalculated for the actual prototype

Joint	Active length of Nitinol (mm)	Curvature radius (mm)	Diameter (mm)	Torque (N.m)
Joint 2	12	7.48	0.89	0.1
Joint 1	20	12.75	0.89	0.06

The effective joint torques are also doubled in this prototype. The second prototype using these parameter values is presented in Figure 4-9:

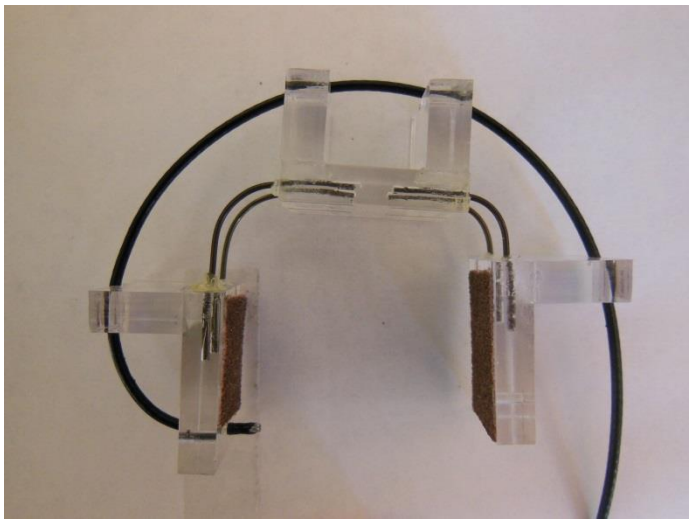

Figure 4-9: Second prototype of the underactuated finger

Chapter 5: Characterization of the PMMA

It is necessary to characterize the PMMA samples in order to know the composition of the thermoplastic used for the prototype and to know if the PMMA is pure or if it was produced using additives, plasticizing or other elements which can change its properties. In general, additives in polymers are used to obtain a specific result (change formability, change pigmentation, resist an external environmental effect, and so on) but in some cases they can alter the molecular structure, and thus the fundamental properties, of plastic polymer materials. Some changes, such as unintentional reduction in molecular weight, can lead to plastic degradation and product failure, while others can supplement or improve a polymer's characteristics. Since we are not exactly sure which material we are facing, it is important to determine if additives have been added and the amount and/or the type included.

The non-destructive analysis method preferred to characterize a polymer is the Fourier Transform Infrared Spectroscopy (FTIR). Materials absorb infrared energy at specific frequencies (or wavelengths) so specific chemical groups of the material are determined by their characteristic vibrations [35]. Thus characteristic vibration allows inference of chemical functions present in the material.

The principle is the following. Molecules in the material will start to vibrate when subjected to energy close to the molecule's vibration energy (corresponding to a specific wavelength). This molecule will absorb radiation and record a decrease in the reflected or transmitted intensity. Infrared ranges corresponding to vibration energy of the molecule extend from 4000 cm^{-1} to 400 cm^{-1}. Not all vibrations give a specific absorption; it depends mostly on the geometry and symmetry of the molecule. Position of the absorption bands will depend, in particular, on the difference of electronegativity and the mass of the atoms involved.

Hence, a material with specific chemical composition and structure will match a series of characteristic absorption bands allowing identification of the analyzed material.

In this technique, Fourier Transform Infrared Spectrometry has been used. The sample receives an infrared radiation, and wavelengths and intensity absorbed by the material are measured.

Two types of information can be obtained from this analysis: qualitative and quantitative.

Qualitative information includes characteristics of the chemical groups present in the analyzed material. In the literature, characteristic frequencies related to characteristic vibrations of different chemical organic compounds have been tabulated, as shown in Figure 5-1.

bond		*type of compound*	*frequency*
–C–H	(stretch)	alkanes	2800–3000
=C–H	(stretch)	alkenes, aromatics	3000–3100
≡C–H	(stretch)	alkynes	3300
–O–H	(stretch)	alcohols, phenols	3600–3650 (free) 3200–3500 (H-bonded) (broad)
–O–H	(stretch)	carboxylic acids	2500–3300
–N–H	(stretch)	amines	3300–3500 (doublet for NH_2)
O –C–H	(stretch)	aldehydes	2720 and 2820
–C=C–	(stretch)	alkenes	1600–1680
–C=C–	(stretch)	aromatics	1500–1600
–C≡C–H	(stretch)	alkynes	2100–2270
O –C–	(stretch)	aldehyde, ketones, carboxylic acids	1680–1740
–C≡N	(stretch)	nitriles	2220–2260
C–N	(stretch)	amines	1180–1360
–C–H	(bending)	alkanes	1375 (methyl)
–C–H	(bending)	alkanes	1460 (methyl and methylene)
–C–H	(bending)	alkanes	1370 and 1385 (isopropyl split)

Figure 5-1: Absorption frequencies of some common bonds [36]

Quantitative information allows, by integrating the peak area of the characteristic signal, to compare the proportion of a chemical group in different samples if the thickness of the layer is already known. It is also possible to know the thickness of the films in relation to each other if the composition of the samples is known. To obtain a precise measure, it is important to calibrate layers with another technique to establish an experimental relation between signal intensity and proportion and/or thickness.

In conclusion, this non-destructive and simple method allows efficiently analyzing organic and inorganic materials. The diversity of experimental installation of the device allow characterization of any type of sampleno matter their physical state and their surface. Attenuated total reflection installation (ATR) allows analyzing layers deposited on non-transparent substrates and polymer films while transmission installation allows analyzing layers deposited on transparent substrates and powders.

The next section discusses the preparation of the samples analyzed using Fourier Transform Infrared Spectrometry.

5.1. Preparation of the samples

Three film samples have been prepared with a hydraulic press and analyzed:

- 1st sample (average thickness: 0.31 mm)

For this sample, a small amount of PMMA has dropped in the hydraulic press between 2 metallic plates previously washed with acetone. Unfortunately, the machine and the plates were not completely clean and some dirty deposits were found in the pressed film. Observation of some bubbles also at the surface of the sample revealed that, the sample was

not completely homogeneous. For a good lubrication and to remove the sample without breaking it, a Teflon spray was used on the both metallic plates.

It is important to be careful about the pressure applied on the sample. Too much pressure from the hydraulic press on a small section could damage the plate or the sample. The purpose of preparing different samples is to obtain the thinnest sample possible required for FTIR analysis. The thinner the sample, the more precise the analysis will be.

Table 5-1: Parameters for the 1st sample

Temperature	Pressure
250°C	1 ton

- 2nd sample (average thickness 0.16 mm):

For the second sample, the process was approximately the same. Instead of Teflon as a lubricant, we used a slice of aluminum around the sample to facilitate its removal. The result was a little bit better despite the presence of bubbles at the surface and some dirty deposits.

Table 5-2: Parameters for the 2nd sample

Temperature	Pressure
250°C	1.5 tons

- 3rd sample: (average thickness 56 µm):

For the third sample, the same process has been repeated except that we increased the pressure. A thin decent sample was obtained with deposits on the center of the sample but not at the extremities, and part of this sample was used to perform the following tests.

Table 5-3: Parameters for the 3rd sample

Temperature	Pressure
250°C	2 tons

Figure 5-2 illustrates the three samples analyzed in FTIR:

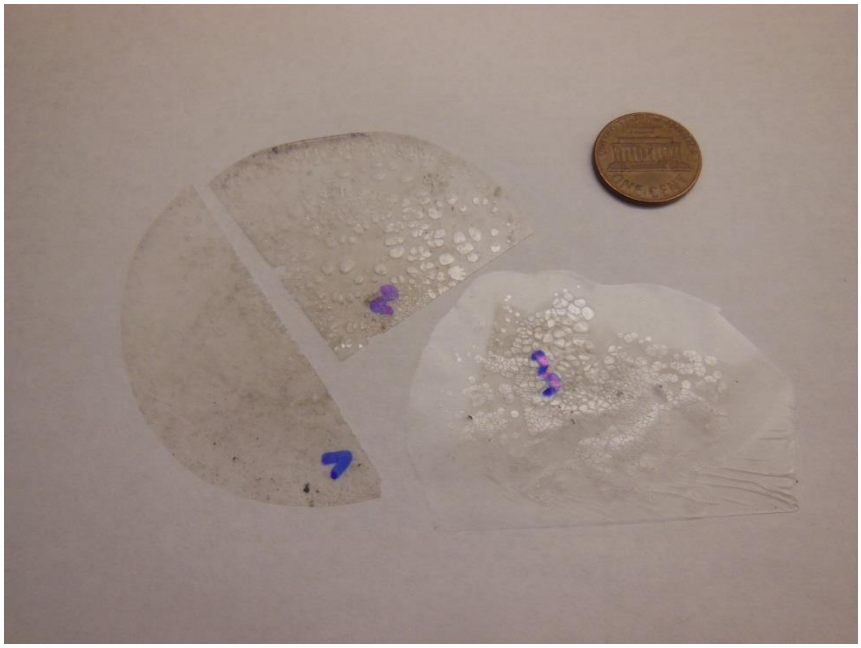

Figure 5-2: FTIR samples

5.2. FTIR Analysis

IR analysis was performed on these three samples. The instrument used is a Nicolet Avatar 360 FT-IR. It is a mid-IR spectroscopy with a maximum resolution of 0.5 cm^{-1}. The parameters of the analysis were presented as follows:

- Number of scans: 16
- Range of frequencies: 4000 to 600 cm^{-1}
- Resolution: 4 cm^{-1}

The first step is to compare the scans of the three samples to make sure that they are similar to each other. The spectra of the three samples are compiled into one in order to be compared, as shown in Figure 5-3:

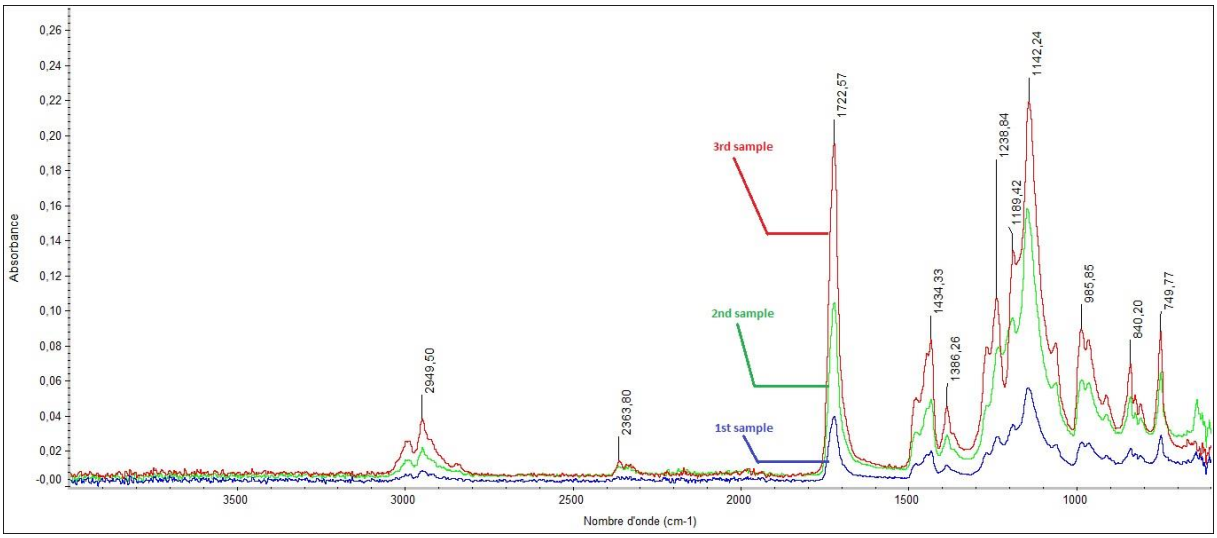

Figure 5-3: FTIR spectrum of the three samples

Spectroscopy analysis shows that spectra of the different samples (1, 2 and 3) have the same features. Peaks are matching for each wavenumber. The preparation, but also the presence of deposits on the sample, does not seem to influence the analysis.

Now, to be sure that the previous spectrum is the spectrum of PMMA and to know if deposits observed on the samples had no influence on the analysis, we have to compare this with the spectrum of PMMA obtained from the database of the OMNIC spectra software. The spectrum of the third sample has been used as a comparison:

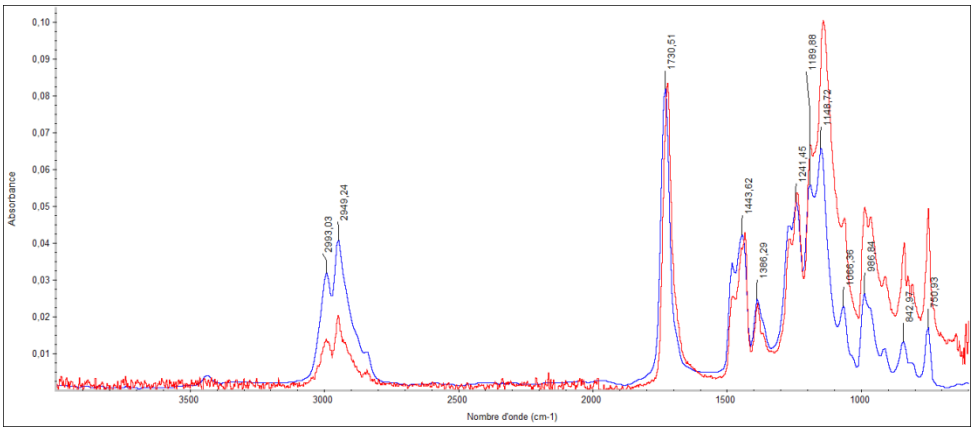

Figure 5-4: Comparison between the third spectrum and the spectrum from the database

The main purpose of this analysis is to identify the different peaks of PMMA and see if it matches with the spectrum obtained from the database. By identifying the different peaks in the spectrum and comparing it to the database, we will be able to tell if the deposits present in the sample have an influence on the analysis or if the PMMA tested is sufficiently clean. If additional peaks appear on the spectrum, these will be characteristic of other chemical groups.

By looking at Figure 5-4, the first obvious conclusion of this second analysis is that the spectra of the different samples (1, 2 and 3) are the same and the peaks also match perfectly with the database peaks of PMMA as shown in Table 5-4.l, this step is not necessary.

We can then affirm that the PMMA tested with infrared spectroscopy is a clean PMMA without additives. So the deposits have no influence on the analysis or otherwise the tested parts did not contain deposits or other foreign additives.

Table 5-4: Table of experimental and database wavenumbers

Database Wavenumbers (cm^{-1})	Experimental Wavenumbers (cm^{-1})
2993.03	2993.47
2949.24	2949.12
1730.51	1721.14
1443.62	1433.71
1386.29	1385.80
1241.45	1283.63
1148.72	1141.41
986.84	985.98
842.97	840.23
750.93	749.77

Another last step should qualitatively confirm the previous hypothesis. Peaks from the analysis and from the database need to be compared using the wavenumbers. Wavenumbers have to match also with the literature. Each frequency range of wavenumber refers to a characteristic chemical group. If a spectrum has been identified to be different from the database, other chemical groups would have to be characterized in order to know which species is/are present inside the PMMA. But since the experimental and database spectra are identical, this step is not necessary.

We can then affirm that the PMMA tested with infrared spectroscopy is a clean PMMA without additives.

Chapter 6: Experiments using the Robotic Finger

6.1. Bench-Top Testing

For the first prototype, force-deflection testing was carried out in a bench-top laboratory environment to validate the basic functionality of the compliant finger. With the finger fabricated to dimensions approximately equal to those specified in Table 4-3, the finger was extended against a force gauge. The maximum grasp force, measured at a fully open finger position, slightly exceeded the target value. Deviation from predicted behavior can be attributed to accuracy of manufacturing. It was also observed that, as intended, the joints displace at approximately the same rate as force was increased, indicating that the stiffnesses are were well balanced across the pair of joints.

Two different tests were performed on the second prototype to demonstrate its efficacy:

- Force-deflection test – measuring the maximal force needed to fully open the finger and consequently the torques carried in the joints
- Grasping test on various objects

The first of these tests aims to indirectly measure joint stiffness by measuring the force required to fully extend the finger. The protocol of this experiment is shown in Figure 6-1.

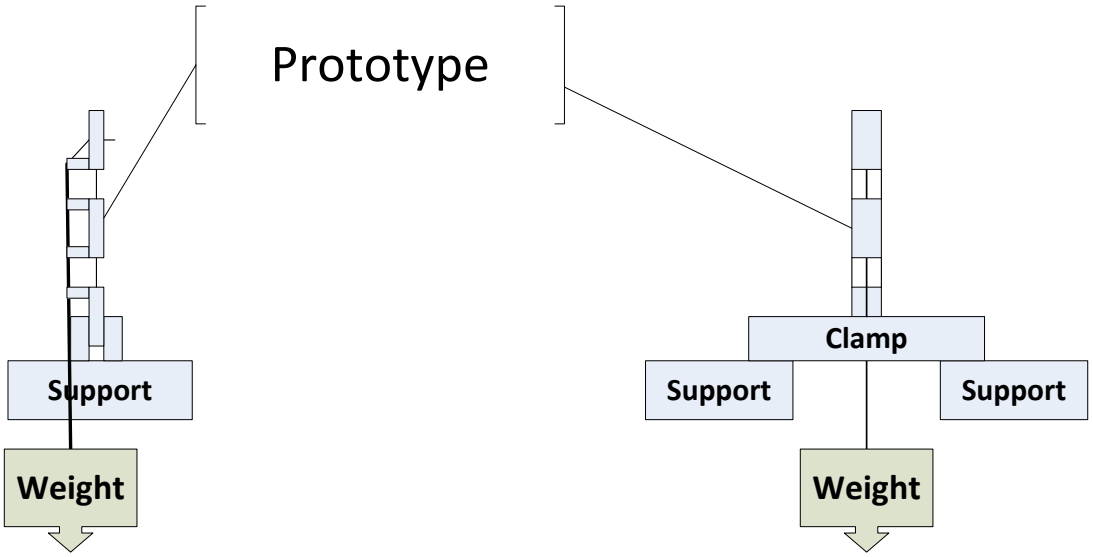

Figure 6-1: Finger load test: side elevation (left), front view (right)

Five tests were performed, resulting in suspended mass measurements averaging 476 g (st. dev. = 74 g; max. = 520 g). Given that:

$$W = m.g \quad (10)$$

The corresponding maximum applied force is approximately 5.1 N. This force can then be converted into moment at the finger joints using the dimensions shown in Figure 6-2 as follows.

$$M_{max} = W_{max}.d = 5.1 * 1.587 = 0.081\ N.m$$

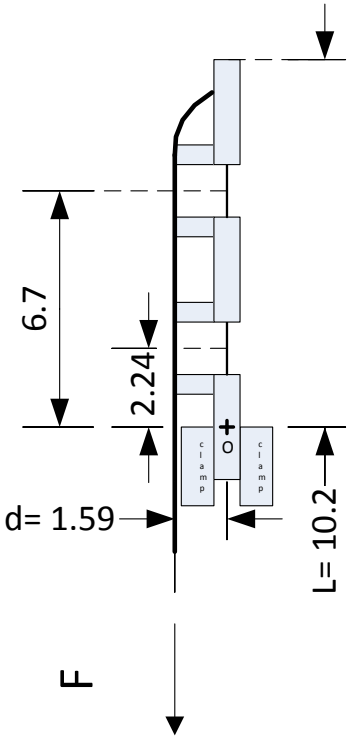

Figure 6-2: Dimensions (in cm) of the prototyped finger

Table 6-1: Comparison between experimental and theoretical values of torque

Joint	Theoretical torque (N.m)	Experimental torque (N.m)	Inaccuracy (%)
Joint 2	0.220	0.081	63%

The values of the torque corresponding to the joint 2 is gathered in Table 6-1 in comparison with the theoretical values calculated based on assumed Nitinol properties. The inaccuracy is seen to be significant, and may be attributable to the following sources:

- Incorrect assumption of Young's modulus or other Nitinol parameters (additional testing could elucidate).
- Accuracy of measurement methods (full extension of the finger is difficult to precisely measure with the current experimental setup).

The second test has to do with practical functionality of the finger. The test consists of grasping objects with various dimensions and stiffnesses. Figure 6-3 shows two successful grasps for large diameters objects. More precisely, the limits of the diameter of the objects that the finger is able to grasp should not be less than 3.5 cm.

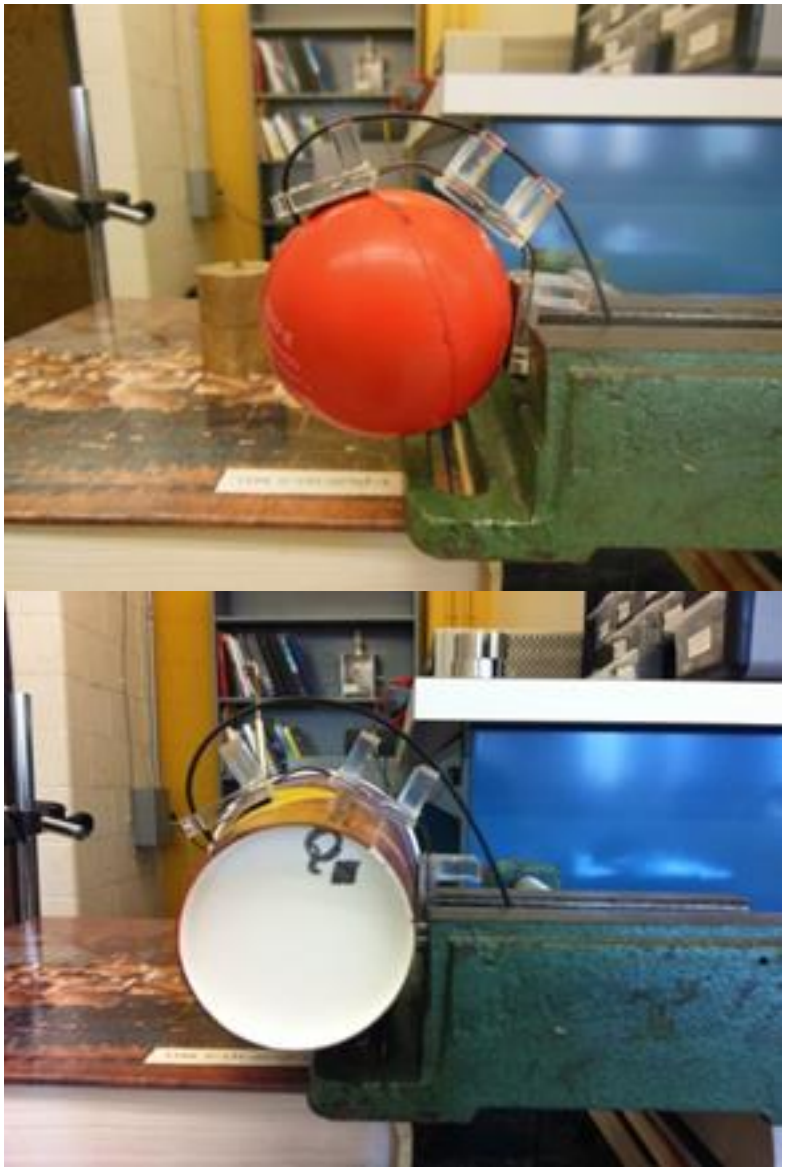

Figure 6-3: Second prototype in grasping mode

6.1.1. Verification of Young's modulus by 3-point bending test

Based on previous testing, the Young's modulus value was assumed constant and equal to 24.9 GPa [37]. But since the value of joint torque is highly dependent on the value of Young's modulus, it is important to verify the value by testing on the Nitinol wire used for the experiments. It appears by looking at the formula below that a lower value of the modulus could lead to a lower theoretical value of the torque and at the same time decrease the inaccuracy compared to the experimental value as previously mentioned.

$$M_0 = \frac{\theta_0 . E . \pi . D^4}{64 . L}$$

A 3-point bending test has been performed on the Nitinol wire. For this we need to consider a beam (NiTi wire) simply supported at its ends with a concentrated load P applied at the center of the beam. The diagram of the experiment is presented in Figure 6-4:

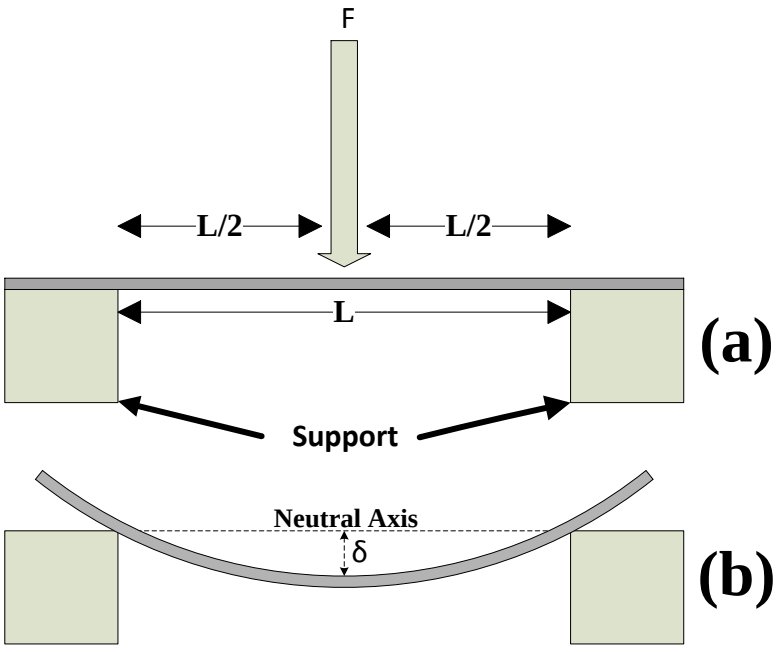

Figure 6-4: 3-point bending test geometry before (a) and after (b) applying load [38]

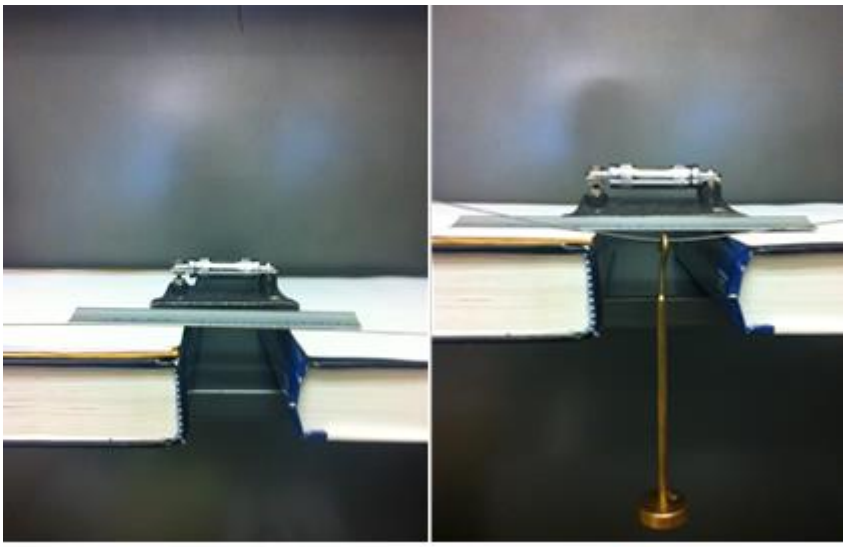

Figure 6-5: Nitinol wire before (left) and after load (right)

The maximum deflection located in the center of the beam is expressed by:

$$\delta = \frac{F.l^3}{48.E.I} \quad (11)$$

with:

- F the force applied at the end of the beam
- l the length of the beam
- E the Young's modulus
- I the second moment of area of the beam cross section: $I = \frac{\pi.D^4}{64}$

and D being the diameter of the section. We can now express the Young's modulus and substitute the expression for the moment of inertia I into the formula (11), which gives:

$$E = \frac{4}{3}.\frac{F.L^3}{\pi.D^4.y}$$

$$E = \frac{4}{3}.\frac{g.L^3.m}{\pi.D^4.y} \quad (12)$$

In order to make a reproducible test, five different masses were used: 50, 100, 150, 200 and 240g. For each mass, five deflection measurements were performed, for a total of twenty-five measurements. Average Young's modulus for each mass has been calculated. All the results can be found in Appendix B. Table 6-2 summarizes the main stiffness values according to the different tests:

Table 6-2: Summary of the average deflection and Young's modulus for the different tests

Test #	Mass (g)	Average Deflection (mm)	Average Young's Modulus (GPa)
1	50	4.56 ± 0.09	15.71 ± 0.29
2	100	7.49 ± 0.36	19.16 ± 0.93
3	150	10.15 ± 0.40	21.20 ± 0.88
4	200	11.87 ± 0.36	24.17 ± 0.74
5	240	17.04 ± 0.88	20.23 ± 1.06

According to the formula, the stiffness should remain constant. The deflection proportionally increases as a function of the mass, so the ratio m/y also remains constant. So we are able to verify if the measurements obtained are following this trend. Figure 6-6 shows the curve $E = f(m)$ describing the behavior of the stiffness as a function of the mass. This curve does not exhibit a constant value of stiffness. One reason is that some irregularities can be noticed for the first and last tests. Indeed, for the first test, since the load is very low, the associated resolution is also low and the readings may not be as accurate compared to the other tests. In other terms, measurements are less precise relative to their magnitude. Concerning the last test, the results are less reliable because the large load leads toward nonlinear behavior, outside the regime of the linear Euler-Bernoulli beam approximations. Geometric nonlinearities occur when deflections are such that they alter the nature of the problem [22].

Examples of geometric nonlinearities are large deflections, stress stiffening, and large strains. In this nonlinear case, we are dealing with large deflections.

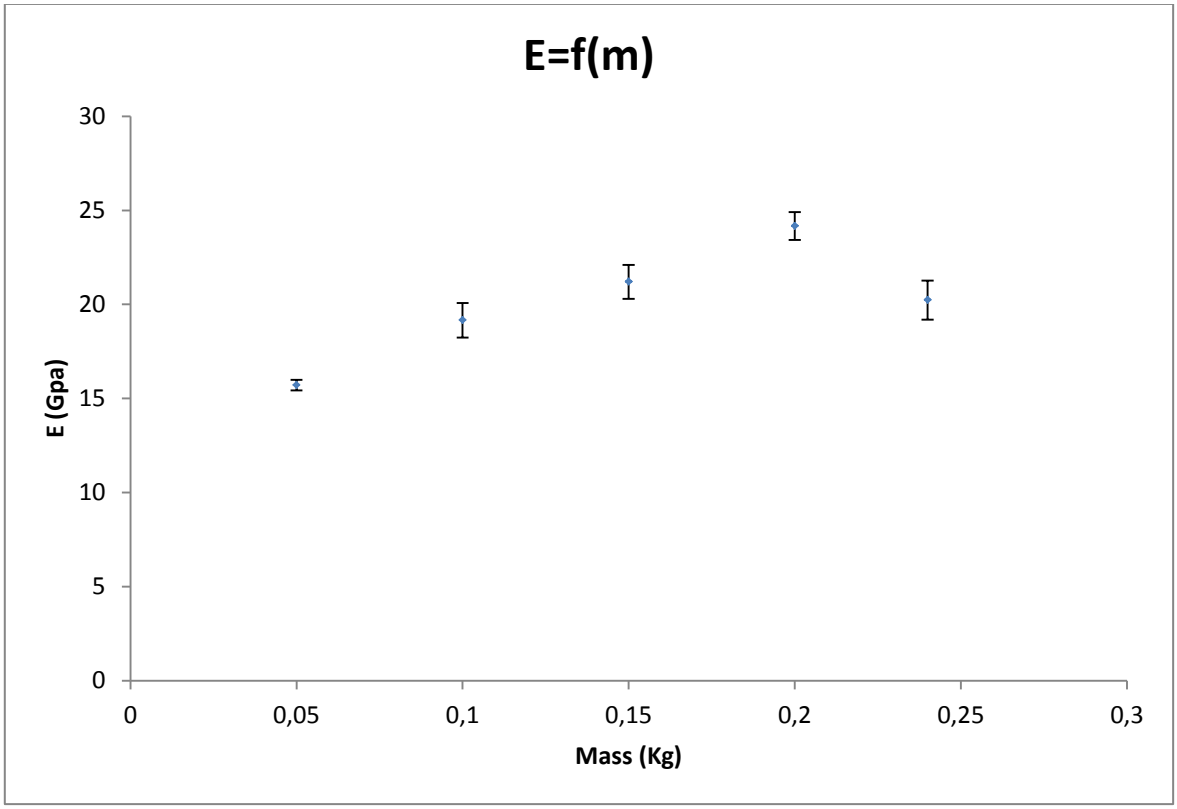

Figure 6-6: Stiffness as a function of suspended mass

To compensate for the low resolution of the first test and the limits of the model, weights have been introduced to calculate the average stiffness of the Nitinol sample. The weight values have been chosen in order to tailor the level of confidence for each test rather than totally discarding data. Weights for tests #1 and #5 are half of the other weights. The formula for the overall average stiffness becomes:

$$E = \sum_{n=1}^{5} E_n \times w_n \quad (13)$$

with:

- E_n the average Young's modulus for the n^{th} test

- w_n the weight imputed for the stiffness values

Subject to $\sum_{n=1}^{5} w_n = 1$

Appendix C shows the set of calculations in order to find the weighted value of stiffness. Results give a stiffness value of 20.6 ± 2.8 GPa. Published average values of E are, for the martensitic phase, between 28 and 41 GPa [30]. Our value of E is a little bit lower but matches well enough with published values. Standard deviation in the case of the weighted sum corresponds to the square root of the weighted variance.

6.1.2. Verification of the theoretical values of the joint torques

In section 6.1.1, the values of torque corresponding to the joint 2 has been calculated in comparison with the theoretical values calculated based on assumed Nitinol properties. The goal here is to calculate the theoretical value using the true value of Young's modulus, which could make the inaccuracy between theoretical and experimental values less significant than was previously understood. Table 6-1 shows the new calculated theoretical values and the associated inaccuracy and Table 6-4 shows inaccuracy before and after the verification of Young's modulus.

Table 6-3: Comparison between experimental and theoretical values of torque

Joint	Theoretical torque (N.m)	Experimental torque (N.m)	Inaccuracy (%)
Joint 2	0.182	0.081	55%

Table 6-4: Comparison of inaccuracys before and after verification of the Young's modulus

Joint	Inaccuracy before (%)	Inaccuracy after (%)
Joint 2	63%	55%

The inaccuracy is decreasing by correcting the value of Young's modulus.

6.2. Interface characterization by pull-out testing

6.2.1. Generalities about pull-out test and metal/polymer interface

For designing a robotic finger prototype, it is important to consider the interface between our NiTi wire and the PMMA. Since the finger will be subjected to significant loads during grasping, we need to characterize our interface regarding these loads. Even if the loads likely to be observed relative to the finger's movement are not completely comparable to the ones undergone when a uniaxial tensile load is applied (similar to a cantilever beam); the preferred technique to characterize the metal/polymer interface remains the pull-out test.

In the case of NiTi coupled with polymeric matrices, the aim is to study the behavior of interfacial adhesion strength between these two constituents.

The adhesion between two surfaces is governed by three mechanisms [39]:

- Molecular bonding (chemical bonding, dipole-dipole interactions, Van der Waals)
- Mechanical coupling, also called mechanical interlocking due to surface roughness which increases the surface area and allows a greater molecular bonding interaction
- Thermodynamic adhesion corresponding to the optimization of the interfacial tension occurring when the surface energy of the polymer is minimized

It is important to notice that these three parameters are highly dependent on the materials and the surface condition of these materials.

The parameter responsible of the interfacial adhesion in our case is the mechanical interlocking. The mechanical interlocking is due to the surface roughness of the materials. To improve interfacial adhesion in NiTi/PMMA composites, we need to increase the surface roughness (for example sandblasting, see below) of the Nitinol. Besides, the increased surface will allow reinforcing the mechanical interlocking during a pull-out test.

In general, metals and polymers don't bond to each other because a lot of interfering modifications occur at the adhesive interface. This depends on the thickness of the interface layer. The bonding of metals and polymers is widely done in industry so is not impossible. But the physical mechanisms and chemical features happening at the interface are only becoming fully understood in the two last decades. In this type of composite, some other phenomena need to be considered to fully understand the difficulty of bonding between these materials.

Regarding the bond formation at the interface, we know that the adhesion is efficient when molecular bonding happens. But since molecular forces are relatively short range, close contact and good wetting conditions are required [40]. In the case of metal/polymer, this interaction is very rare.

Polymers have poor wettability due to their low surface tension γ. The surface tension for PMMA is about 41.1 mN/m [41]. Furthermore, metallic oxide surfaces may exhibit topology which makes contact with molecules problematic.

Improvement of interface adhesion between metals and polymers could be done using: polymers with low viscosities, thermal stimulation of molecular mobilities (i.e., thermoplastic adhesives), and polymer surface excitation to increase functional reactive groups (hydroxyl, hydroperoxide, carboxylic species) by flaming, corona discharge or even plasma treatment [40].

Another example of interfacial adhesion improvement is the chemical functionalization of polymer surfaces by grafting. In this example, a polypropylene film is grafted with acrylic acid after an oxidizing aluminum beam (by electron radiation), resulting in a surface copolymer with polyacrylic acid [42].

In specific cases like this, chemical bonds can be generated through two kinds of forces [40]:

(1) The Van der Waals forces originate form molecular dipole interactions. When integrating over two approaching surfaces, they turn out to be a weak but long range interaction

(2) Acid-base phenomena involve all charge transfer reactions: hydrogen bonding and the electron pair interactions (covalent and ionic bonding). In the previous case exposed above [42], it has been shown that hydrogen bonds formed between the (polymer) carboxylic and the (oxide) hydroxyl groups are prevalent. It has been also shown that interface formation has been made, characterized by an infrared absorption.

The pull-out test has been widely used in the past to measure the needed force to pull a fiber of a known length out from a matrix. This force can be measured by performing a uniaxial tensile load to a fiber embedded in a matrix.

Previous studies have been focused on pull-out tests using samples made from the shape memory alloy NiTi and polymeric matrices. Since interface adhesion between polymers and metals are not as good as desired, different surface treatments can be carried out in order to improve the interfacial adhesion strength. Several of these treatments deal with treating NiTi samples by etching, hand sanding or sandblasting [43, 44] or polymer coating [45]. Among these treatments, it appears that sandblasted wires possess the strongest adhesion [43] and a lower wire displacement [45]. Another treatment involves using silane couple agents on NiTi wire surfaces to improve the adhesion strength [46].

The adhesion strength can be determined according to different normalization. In each study, the purpose of pull-out tests is to measure the maximum force needed for an adhesion failure, meaning the force needed to create a debonding between the fiber and the matrix. But the adhesion strength is a normalized value obtained by dividing the maximum debonding force

over the embedded geometry of the fiber. The force can be divided either by the embedded strip area [39] either by the embedded length of the wire [46].

Since the geometry of the sample used in this study remains the same, we can consider the adhesion strength (σ_m) to be proportional to the maximum force reached before complete debonding (F_m) divided by the embedded length (L) of the fiber:

$$\sigma_m = \frac{F_m}{L} \quad (14)$$

This means that the higher the adhesion strength of the sample, the better the adhesion is.

The schematic curve of normalized adhesion strength vs. deflection of a pull-out test can be shown in Figure 6-7.

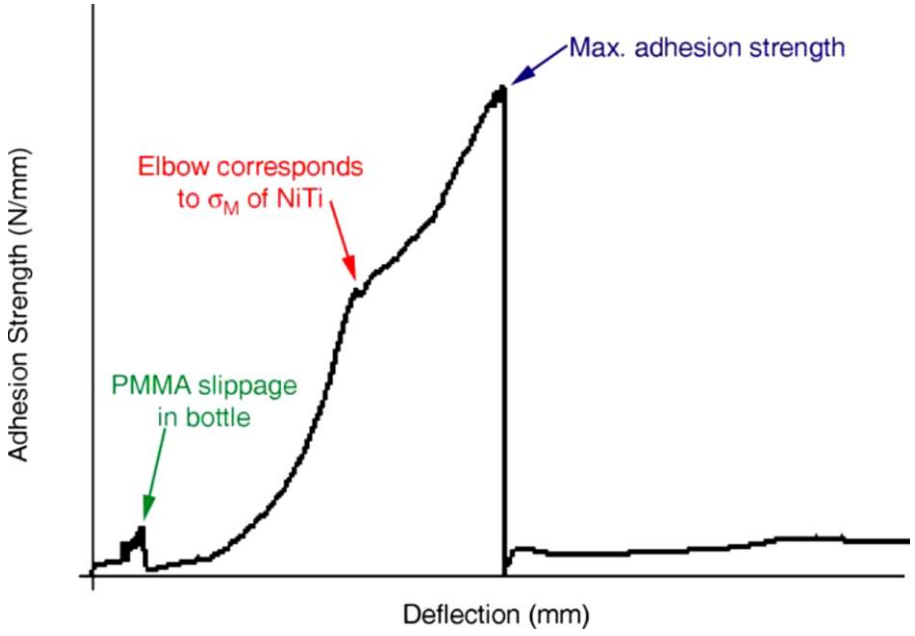

Figure 6-7: Characteristic curve of pull-out test on NiTi/PMMA sample [46]

This curve is representative of a treated PMMA/NiTi sample with a certain sample preparation. Some phenomena due to constraints on the PMMA or on the wire could be

observed but the interpretation of the curve stays unique depending on the materials, the sample preparation and the surface treatments applied on the sample.

In order to compare experimental values to values coming from literature, we can introduce the formula of the interfacial shear stress, involving the section of the fiber (2πr), which gives a normalized value in MPa. The formula is:

$$\tau_m = \frac{F_m}{2\pi r L} \quad (15)$$

6.2.2 Preparation of the samples using two techniques

The study presented in this part will allow choosing between two different techniques to combine polymer/metal alloy in order to further create the robotic finger.

For the different tests, half a phalanx of a clear cast PMMA (Mc Master-Carr, Elmhurst, IL) was used. A 0.89 mm untreated, straight shape memory Nitinol wire (Memry, Bethel, CT) was used.

Figure 6-8 shows an example of a pull-out sample. The processes to obtain these samples are explained in the following sections.

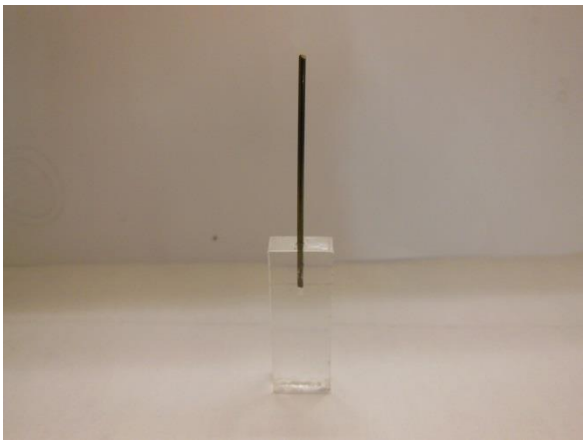

Figure 6-8: Example of pull-out test sample

The two methods considered are a friction process and a coupled friction/heating process. The pull-out test will be used to characterize the adhesion between PMMA and NiTi wire, and unlike previous studies, where the purpose was to compare the adhesive strength between treated and untreated metal alloys, this method will be aimed at comparing the different techniques to each other and see which one is the more adapted to join these elements.

- 1st process: friction

Before putting both parts together, the first step is to pre-drill a hole. The pre-hole, which is smaller than the Nitinol diameter ($\frac{1}{32}$ in), is drilled in the PMMA in order to facilitate the insertion of the Nitinol by friction. A sketch of the sample is shown in Figure 6-9:

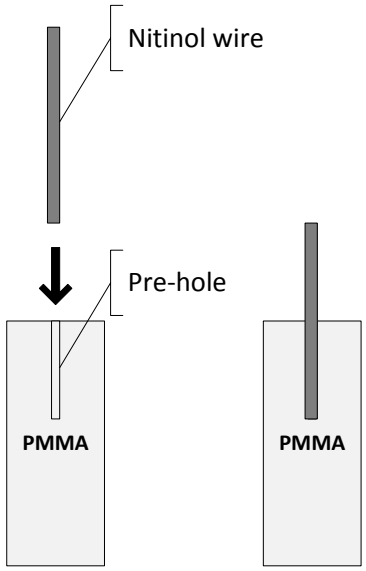

Figure 6-9: Sketch of the insertion of the Nitinol into the PMMA

Figure 6-10: Drilling of PMMA

Typically here, the friction is the force resisting the relative motion of material elements sliding against each other. In this case, the friction phenomenon is a dry friction because it is involving lateral motion of two non-lubricated materials in contact. We could be even more precise and say that is a “dry kinetic friction” because this friction happens between two moving surfaces [47].

Once the drilling of the pre-hole has been done, the drill press was used for facilitating insertion. The upper part of the drilling machine was used to fixture the Nitinol, which is easier because the diameter is almost the same as a typical drill bit.

Figure 6-11: The drilling machine

The lower part of the machine is used to hold the PMMA component. The goal of this machine is to provide enough force to insert the Nitinol straight into the PMMA.

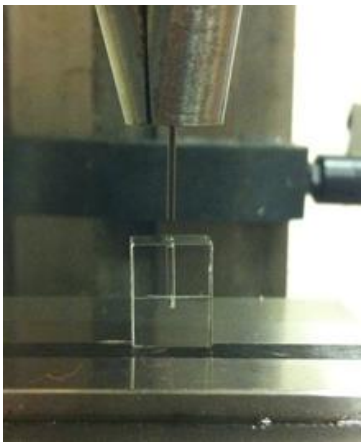

Figure 6-12: Nitinol Insertion into the PMMA

Despite the fact that the friction technique is a good technique above several level (good adhesion interface, low cost, fast, and few tools needed), it shows an adverse effects on the polymer during the introduction of the wire. When the pre-hole is drilled, some material is agglomerating at the bottom of the thread. By pushing down, the wire compresses the material

and causes a lot of constraints in addition to the one related to the introduction of the wire. All these constraints lead to the propagation of cracks inside the PMMA as shown in Figure 6-13.

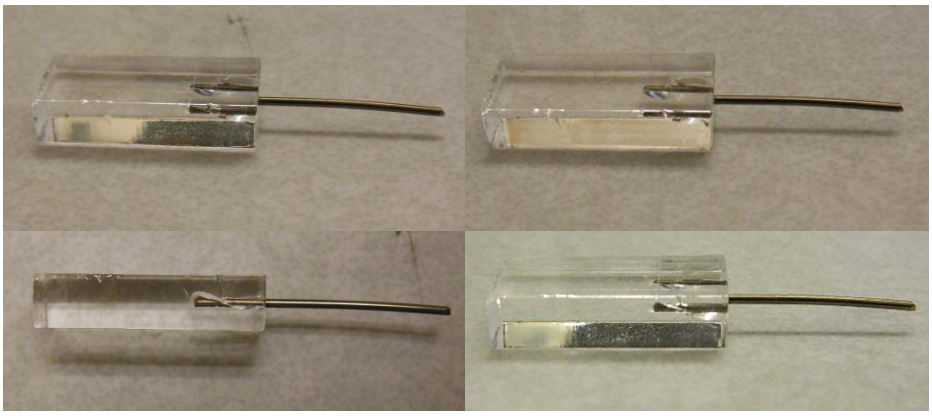

Figure 6-13: Crack observation in the polymer

- 2nd process: Heating and friction

This process is quite similar to the first one except that during the descent of the upper part of the drilling machine, we apply heat on the Nitinol wire using a typical soldering iron (800°F), which makes the friction effect less important than before because a smaller friction force is needed to introduce the wire.

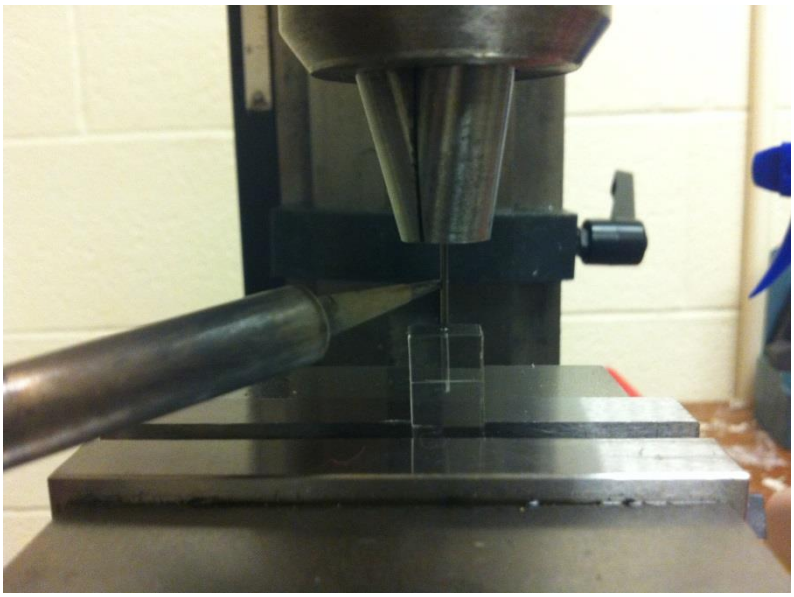

Figure 6-14: Application of heat during the slope down of the superior part

By applying heat at the base of the wire, the polymer melts and it should form around the wire.

Figure 6-15: Sample obtained with friction and heat

Now, both processes need to be tested in order to choose the best technique for prototyping the finger.

6.2.2. Results of pull-out testing

As previously discussed, the best way to choose one of the two previous techniques is to quantify the adhesion between NiTi wire and the PMMA matrix using a pull-out test.

Tests were conducted on a BOSE® ElectroForce® 3200 with a constant load rate of 0.1 N/s until a maximum load of 200N[2] and on an MTS Instron tensile machine with the same constant load rate until a maximum load of 500N. Also, values were normalized using the formula of adhesion strength and compared with values of interfacial shear strength found in the literature, and the embedded length was measured for each sample.

Fourteen tests were performed. In the interest of clarity, each odd test corresponds to a friction test and each even number corresponds to a friction/heating test. Below is the table of the embedded lengths by sample:

[2] The maximum applied load doesn't reach the level needed to induce permanent deformation (just martensitic twin rearrangement)

Table 6-5: Table of embedded length by sample

Test #	Observation	Embedded length (mm)
Test #1: Friction	cracks	7.27
Test #2: Friction/Heat	/	7.73
Test #3: Friction	cracks	7.83
Test #4: Friction/Heat	/	6.41
Test #5: Friction	cracks	6.11
Test #6: Friction/Heat	/	5.86
Test #7: Friction	cracks	6.32
Test #8: Friction/Heat	/	6.18
Test #9: Friction	cracks	6.34
Test #10: Friction/Heat	/	5.90
Test #11: Friction	cracks	6.57
Test #12: Friction/Heat	few cracks	6.08
Test #13: Friction	cracks	6.53
Test #14: Friction/Heat	few cracks	6.65

Figure 6-16 is the result corresponding to an adhesion only made by friction. For this first test we performed a displacement control set up to 0.01 mm/s. The maximal load recorded is 175.42N corresponding to a normalized load of 24.13 N/mm (associated to a displacement max of 0.324 mm). The curve shows a step starting from 0.155 mm at a load of 14.59. This step is most probably due to a slipping of the wire into the matrix. As it has been said, it's not due to a load which can induce permanent deformation because the load is too applied is too low.

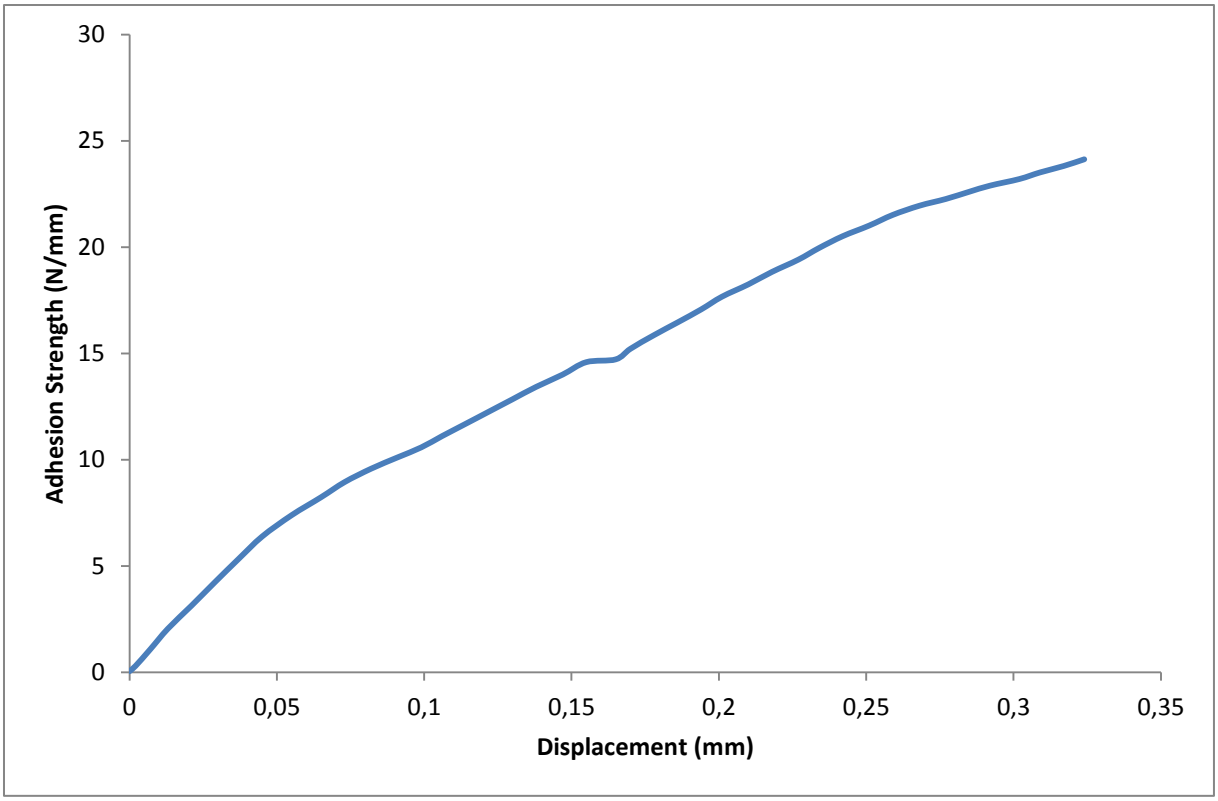

Figure 6-16: Adhesive strength in function of the displacement for the friction test #1

For test #7 presented in Figure 6-17, the protocol was changed. Indeed, parameters for pull-out testing were not well suited to the samples, because the clamps holding the sample were vibrating too much. So instead of a displacement control, allowing a 6 mm displacement maximum, we used a load control with a load rate of 0.1 N/s with a load value of 215 N instead of a previous maximal load value of 200 N. The data for test #7 recorded a maximum load of 167.05 N corresponding to a normalized load of 26.43 N/mm (associated with a maximum displacement of 0.241 mm).

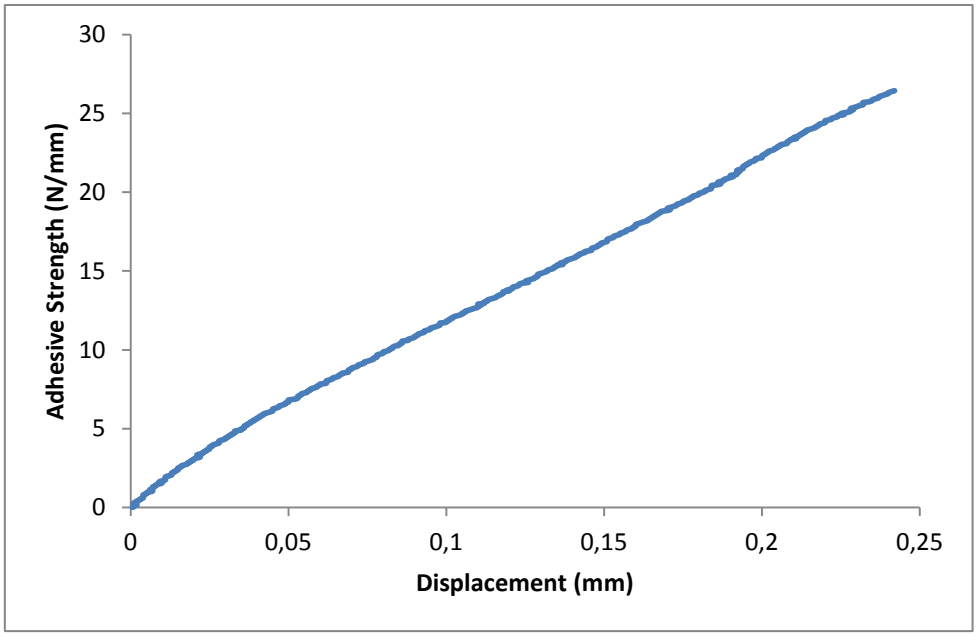

Figure 6-17: Adhesive strength in function of the displacement for the friction test #7

Test #9 recorded a maximal load of 215 N, which is the maximal load allowed by the machine. Indeed, for this sample we had no debonding between the wire and the PMMA, even though the limit of the machine was surpassed.

Because of this, another test has been performed using a MTS Instron tensile machine with the previous parameters (load control of 0.1 N/s) with a maximal load of 500 N (maximum load for the tensile machine: 25kN). This gave interesting results, with curves similar to characteristic curves of pull-out tests. Figure 6-18 shows the curve obtained for test #9 using the larger tensile machine. It shows a displacement step corresponding to the slipping of the wire in the PMMA matrix. The maximal load recorded is 165.49 N corresponding to a normalized load of 26.10 N/mm (associated with a maximum displacement of 0.180 mm). By comparing test #9 to Figure 6-7, the characteristic curve of pull-out test for NiTi/PMMA composites, we can say that the curves are similar.

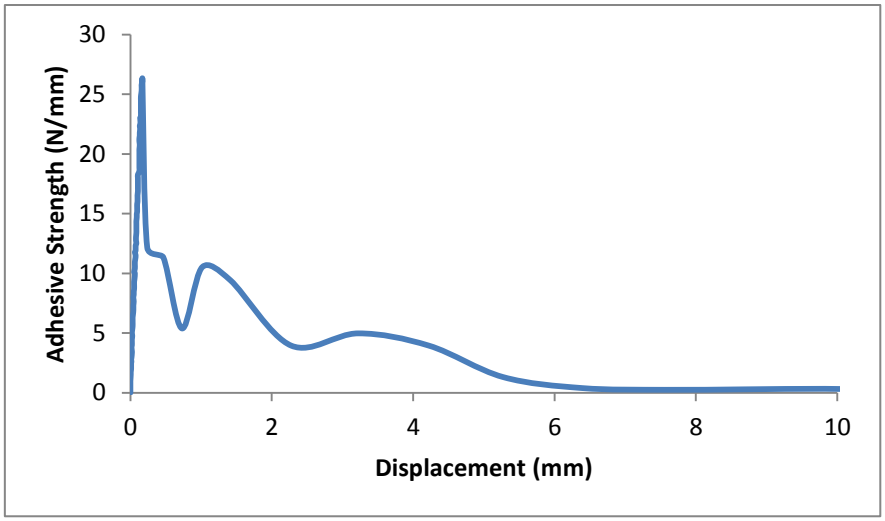

Figure 6-18: Adhesive strength in function of the displacement for the friction test #9

Results of all friction tests have been gathered into one plot for comparison. In order to compare the trends of the curves, only the linear part is plotted until the maximal recorded adhesive strength:

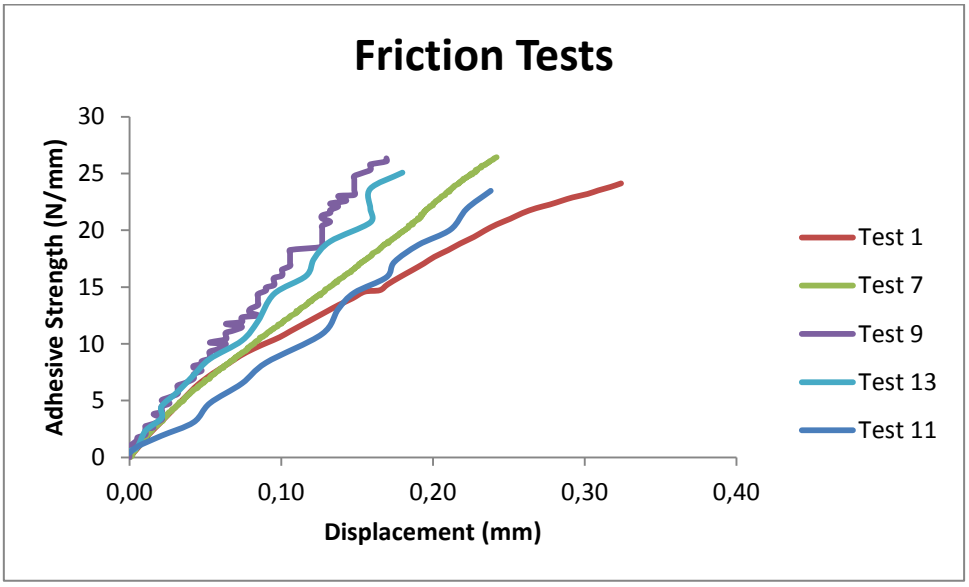

Figure 6-19: Plot of the adhesion strength in function of the displacement for all the friction tests

Values of the maximal adhesive strength have been calculated with the previous formula and reported in Table 6-6. The average maximal adhesive strength with standard deviation has been calculated:

Table 6-6: Data obtained for the friction tests

Samples manufactured only by friction			
Test #	**Displacement Max (mm)**	**Maximal σ_A(N)**	**Normalized Maximal σ_A (N/mm)**
1	0.324	175.42	24.13
7	0.241	167.05	26.43
9	0.180	165.49	26.10
11	0.249	152.52	23.21
13	0.180	163.76	25.08
Average	**0.235**	**164.85**	**24.99**
Std. Dev.	**0.060**	**8.22**	**1.34**
$\boldsymbol{\sigma_m = 25 \pm 1.3\ N/mm}$			

The next results correspond to an adhesion made by friction and heating. For test #4, with the same protocol as test #1, the Bose machine seemed to reach its limit. The maximum load cell available for the Bose is 225 N. The first hypothesis was that the heating of the sample provided too much adhesion, so it was difficult to obtain a value of adhesive strength for this test. In order to validate this hypothesis a second test was performed with same parameters as the friction tests (load rate of 0.1 N/mm and a maximum load of 215 N), using the Bose machine.

Figure 6-16 is the experimental curve for test #4. The maximal load recorded is 79.49N corresponding to a normalized load of 12.40 N/mm (associated to a maximum displacement of 0.139 mm). This test shows that the maximal adhesive strength for the 2nd method is lower than for friction tests. Forming the PMMA around the Nitinol wire is not improving the

adhesion between NiTi and polymer. The friction method allows a better mechanical interlocking between the PMMA and the NiTi wire. This tendency needs to be verified with other tests. Curves obtained for this method are very similar to the curves previously obtained.

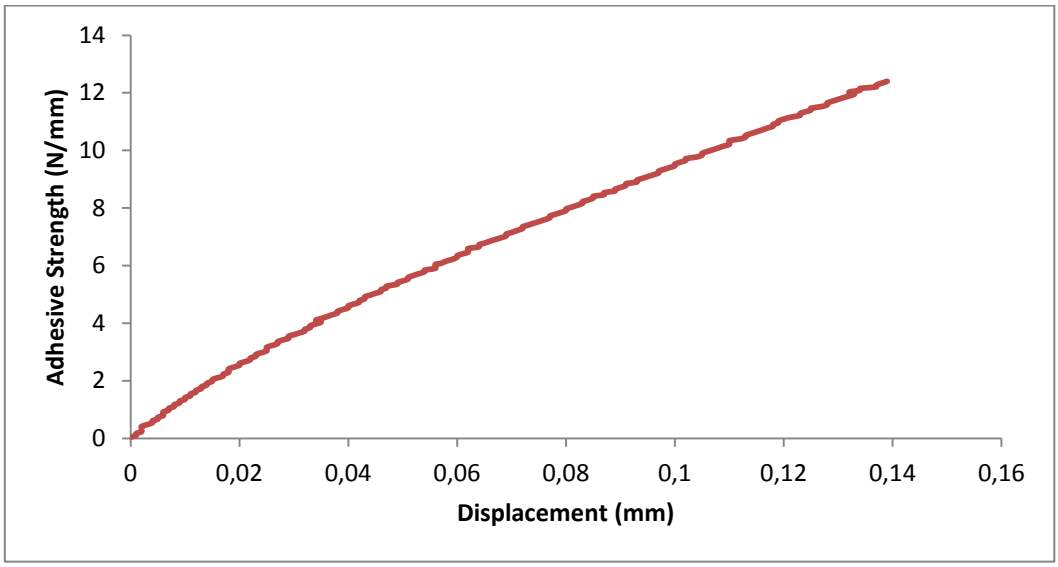

Figure 6-20: Adhesive strength in function of the displacement for the friction/heating test #4

Figure 6-21, corresponding to the curve of test #10, is not a typical pull-out test curve. This curve shows many displacement steps during the increasing of the load. These steps occur at about 0.093mm, 0.132mm, 0.313mm, 0.506mm, and 1.676mm in displacement. As in the first test, the displacements are certainly due to a slipping of the NiTi wire in the PMMA matrix.

On the other hand, the curve shows an improved maximal adhesive strength competing with the maximal adhesive strength for the friction samples. This paradox may be a consequence of a different sample preparation.

Indeed, some complications occurred. The wire was not inserted in one continuous process into the matrix. Cycles of heating and cooling occurring during the preparation of the sample and the matrix did not correctly form the PMMA around the wire. It should have improved the surface roughness, increasing the mechanical interlocking between the two materials and inducing a better adhesion.

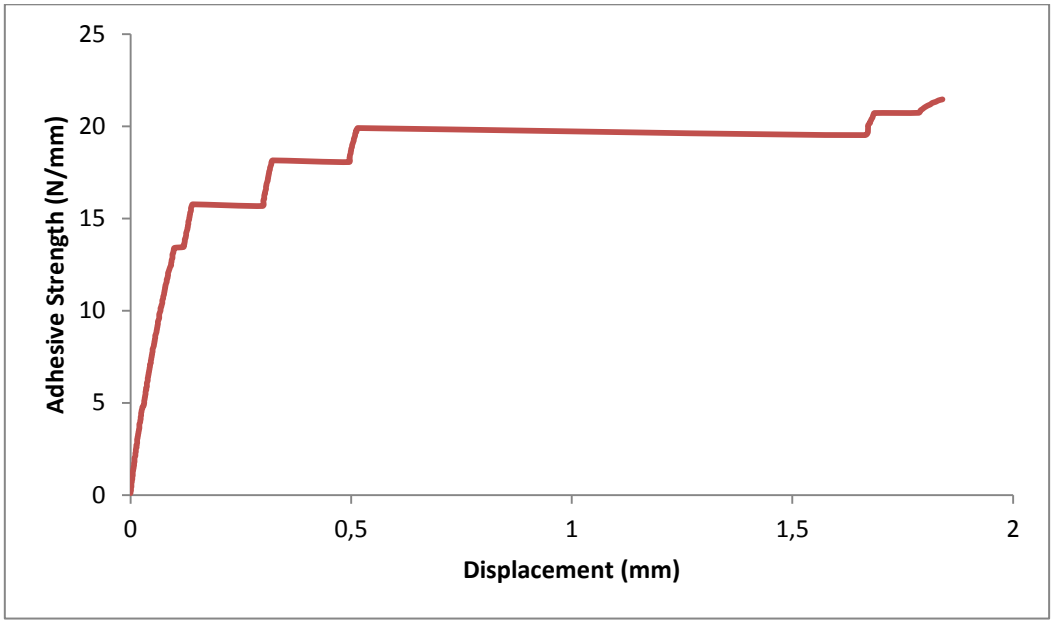

Figure 6-21: Adhesive strength in function of the displacement for the friction/heating test #10

All the friction/heating tests, except test #10, are reported in a single plot for comparison:

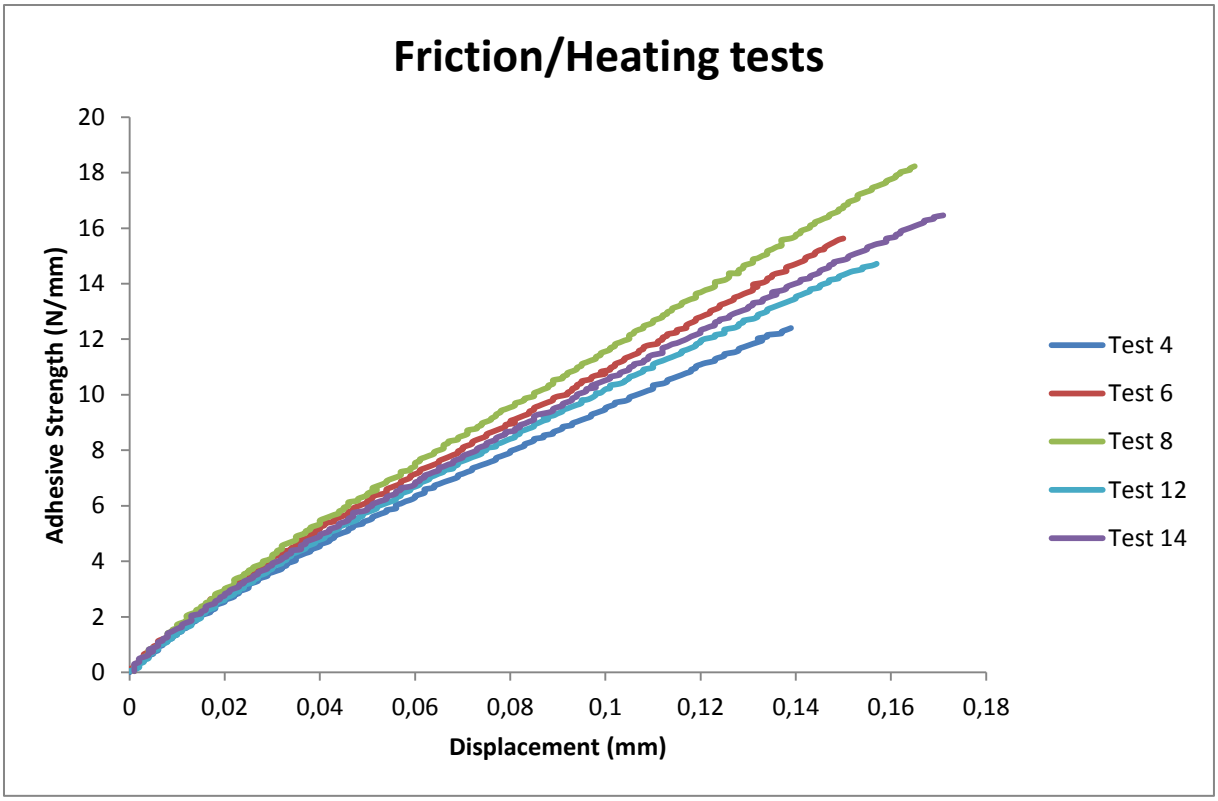

Figure 6-22: Plot of the adhesion strength in function of the displacement for all the friction/heating tests

All the curves show the same tendency, except for test #10 which was explained previously and removed to be analyzed separately. All the values of maximal adhesive strength are reported in a table in order to clearly present the average adhesive strength and the standard deviation:

Table 6-7: Compilation of all the adhesive strength values for friction/heating tests

Samples manufactured by heating & friction			
Test #	**Displacement Max (mm)**	**Maximal σ_A(N)**	**Normalized Maximal σ_A (N/mm)**
4	0.139	79.49	12.40
6	0.150	91.58	15.63
8	0.165	112.65	18.23
12	0.157	89.48	14.72
14	0.171	109.47	16.46
Average	**0.156**	**101.54**	**15.50**
Std. Dev.	**0.010**	**17.58**	**2.20**
$\boldsymbol{\sigma_A = 15.5 \pm 2.2\ N/mm}$			

In conclusion, we could say that the load required to overcome the interfacial adhesion, also called adhesive strength, is more significant for the friction method, compared to the friction/heating method, as shown in Table 6-8 and Figure 6-23.Forming the PMMA around the Nitinol wire does not exhibit the best results of adhesive strength. However, the friction method presents an inconvenient drawback. During insertion of the wire by friction, cracks in the matrix appeared which compromise the efficacy of the method, even considering the high adhesive strength. Other materials could be considered to avoid these inconveniences, such as polycarbonate, which presents better mechanical properties and also good adhesive strength [39], and other methods such as sandblasting could further improve mechanical interlocking and thus interfacial adhesion.

Table 6-8: Summary of the average adhesion strength for the both methods

Method	**Adhesion Strength (N/mm)**	**Standard Deviation (N/mm)**
Friction	25	1.3
Friction/Heating	15.2	2.2

Another interesting study showed that depending on the polymerization of PMMA and also depending on the treatment of the NiTi wires, adhesion could be improved. The main concept of the study was to attach chemical species to the surface of the NiTi wires using silane coupling agents [46]. Better adhesion is shown for UV cured (and vacuum) polymer samples using AIBN initiator prepared with APTS coupling agents (close to 25 N/mm). Also, thermally cured polymer samples using AIBN initiator but prepared with MPS or APTS silane agent show the same good adhesion strength (close to 15 N/mm).

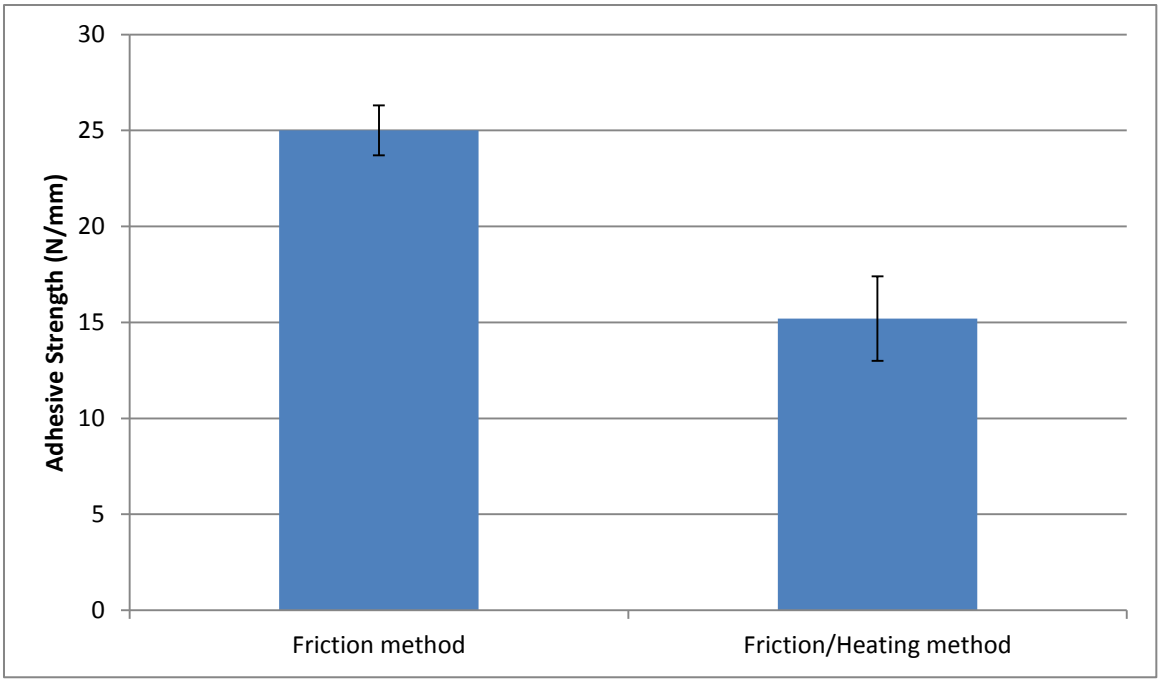

Figure 6-23: Comparison between adhesion strength between the two methods

It could be interesting to compare results of this method to treated composites using the formula of the interfacial shear stress.

Table 6-9: Comparison of both methods using interfacial shear stress formula

Method	**Shear stress (MPa)**	**Standard Deviation (MPa)**
Friction	4.47	0.24
Friction/Heating	2.77	0.39

Different studies have been made on treated or untreated NiTi/polymer composites. It is possible to compare the values according to these studies. Calgano et al. studied the key factors in the fracture of an inclusion within a polymer/metal alloy strip composite during calendaring (cold rolling and folding) using different choices of inclusion metals (Ti alloy or NiTi shape memory alloys) [39] [48]. Polymers used in this study were polycarbonate (PC), polypropylene (PP) and high-density polyethylene (HDPE). Results showed a better adhesion strength between NiTi and Ti with polycarbonate (4.42 ± 0.17 and 4.48 ± 0.27 MPa).

Interfacial bonding adhesion for HDPE/NiTi was lower but close to the result for the friction and heating method (2.26 ± 0.31 MPa). Lower adhesion was demonstrated for PP/NiTi composites. It is also important to note that a fatigue test would be useful as future work to more closely characterize the limiting factors of the joint design.

6.3. Friction tests

Grasping capabilities expected from the design of our underactuated robotic finger, depend not only on the design itself based on compliant mechanical structures (using superelastic joints), but also on the integration of soft friction pads at the fingertips. Increasing the surface friction of the fingers is key to improve grasping abilities. The choice of the pad material as well as the thickness which will provide a good combination of friction and compliance properties is of primary importance [49]. Compliance of the pads will allow a robust and stable grasp in the case of basic grasping sequences because of their conformability and the enlarged contact area [49, 50]. It also allows to “damp dynamic effects” caused by vibrations or shocks, or else dissipate potential strains of the material during grasping. Also, generally compliant materials as polymers possess good friction coefficients, allowing them to use lower gripping forces [50]. Enhanced surface area obtained by deformation of the polymer involves kinematic coupling between the fingertip and the object, facilitating a good grasp of the object. In the case of basic grasping as our robotic finger has been made for, soft pads are well suited. Examples of friction coefficients of different polymers against bearing steel are shown in Table 6-10.

Table 6-10: Friction coefficients for different polymers [51]

Base Material	M
Polyamide 66	0.57
Polyoxymethylene (POM)	0.45
Polyether ether ketone (PEEK)	0.49
Polyethylene terephthalate (PETP)	0.68
Polphenyle sulfide (PPS)	0.70
Polyetherimide (PEI)	0.43

Despite the important characteristics soft pads can exhibit, they also present drawbacks: a visco-elastic non-linear behavior which is difficult to model and a potentially defective grasp induced by low precision or inappropriate stiffness. The visco-elastic model has been inspired from the study of human finger behavior. From previous studies [52, 53], the human finger exhibits a non-linear mechanical behavior caused by the presence of the bone and the nail constraining the deformation of the soft tissues. Because of this, stiffness changes as a function of the flattening of the pad. When the pad is flattened, a non-linear behavior of the stiffness is observed. So the stiffness of the finger depends on the contact area which in turn depends on the grasping force of the finger.

As has already been described, the model of the finger is taken from the biological model; it consists of a rigid body covered with a soft pad layer as shown in Figure 6-24.

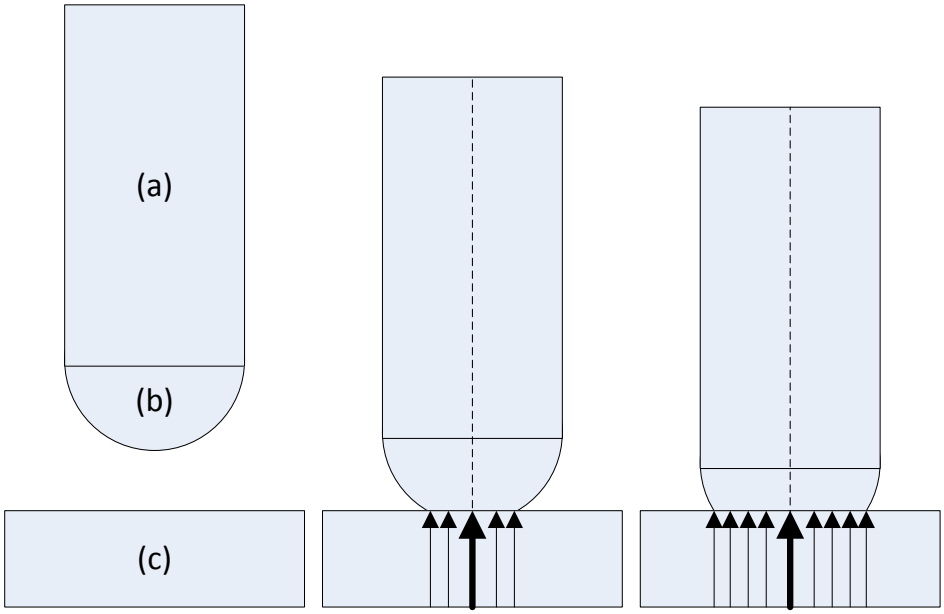

Figure 6-24: Robotic finger consisting of a rigid inner body (a) recovered by a soft pad (b) in contact with an object (c)

In this project, silicone pads made from dimethyl-methylvinyl siloxane elastomers have been used on the finger surface. Slightly different from Figure 6-24, the last phalanx of the finger consist of a rigid inner body (PMMA) entirely covered by a soft pad (silicone).

6.3.1. Preparation of the samples

Different PMMA samples covered with different thicknesses of MED-2014 silicone (Nusil Silicone Technology, Carpinteria, CA) were prepared. PMMA samples were dipped into the liquid in a way to avoid entrapping bubbles on the surface of the form. Samples were rotated for about 5-10 minutes to evenly coat the form and were left to dry for three hours. This is how the first layer was created. Each layer of silicone obtained by dipping is 0.002" thick. To obtain thicker samples, the previously mentioned steps need to be repeated.

Samples with thicknesses of 0.004 and 0.008 inches were prepared. The final step of preparation consists of leaving samples for 10 to 14 hours and then curing them for 60 minutes at 50°C and then at 150°C during 60 minutes.

After complete curing of the silicone on the PMMA, frictional properties of the silicone were tested. Quantifying the frictional force generated between the silicone pad and different materials tested for different amounts of normal force applied and using different thicknesses of silicone allows characterization of the gripping behavior, to know if silicone pads will generate sufficient friction when fingers will grasp objects made from different materials. The testing setup is shown in Figure 6-25.

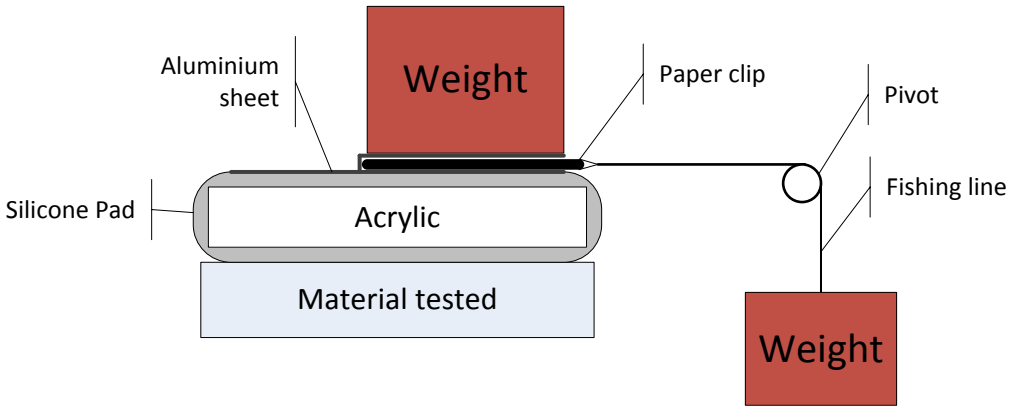

Figure 6-25: Friction test setup

After the PMMA was covered by the silicone pad, an aluminum sheet was glued on the top of the sample, to facilitate re-use of the samples. Over this aluminum sheet a paper clip was glued using Loctite 4014 instant adhesive. A similar aluminum sheet was glued over the paper clip to maintain it. Then normal force was applied uniformly by positioning weights on top of the sample. Weights were added at the other extremity, down to the pivot, until loss of grip was reached.

6.3.2. Results

Three different materials were chosen to be tested against silicone pads: wood, PMMA and steel. For each material, for the sake of gauging repeatability, 3 different normal forces were used: 1.962 N, 3.924 N and 4.905 N (corresponding to 200, 400 and 500g). These tests were performed for two different thicknesses of the silicone pad: 0.004” and 0.008”

respectively corresponding to two or four deposited silicone layers. The detailed calculations for the tests performed on the 0.004" and 0.008" thick pads are shown in Appendix F and G. By comparing friction between the different materials for the first thickness, we notice that higher friction is obtained for PMMA material as shown in Table 6-11.

Table 6-11: Friction coefficient for the three different materials for a 0.004" thick silicone pad

PMMA	Wood	Steel
1.14 ± 0.04	0.88 ± 0.06	0.75 ± 0.04

Also, the silicone used for the experiments and for the fingers provides a good friction coefficient according to the tested materials which means that for a variety of objects, the finger will show improved grasping capabilities with pads versus without.

Now we want to compare these results to the coefficient of friction for a higher thickness. For the second test, using the PMMA, only one normal force was used (400g). Experiments were unsuccessful for the other normal forces. In the same context, using steel as a friction support, only two normal forces were used (200 and 400 g). Results for the second tests are shown in Table 6-12.

Table 6-12: Friction coefficient for the three different materials for a 0.008" thick silicone pad

PMMA	Wood	Steel
2.17 ± 0.16	0.99 ± 0.09	1.58 ± 0.09

Overall, by increasing the thickness from 0.004" to 0.008", the friction coefficients are increasing which means that friction forces are also increasing. It can be inferred that the higher the thickness of the silicone pads, the higher the friction will be (up to some limit). Complementary tests need to be performed, to measure friction on irregularly shaped objects,

in order to demonstrate improved contact is valid not only on flat surfaces. In comparison, silicone materials show typical coefficient values from less than 0.25 to more than 0.75 [54], which makes this material successful for this application.

Chapter 7: Conclusions & Future Work

In this thesis, a new kind of underactuated robotic finger mechanism was presented. This finger was designed to be compliant while providing significant yet controlled grasping forces in either pinching-type or enveloping grasps. Necessary improvements include implementation of a compact actuator system and position sensing feedback. The possibility for integrated sensing of joint angles and pressures on the phalanges is also a potential advantage of the new design but needs further development. The determination of grasp shape and phalanx pressure maybe relatively straightforward. The use of compliant wire joints lends itself to integration with slender electrogoniometers. These flexible wire-like devices are based on miniature strain gauges on a compliant composite wire and can be mounted alongside the finger spanning the joints. Piezoresistive film sensors can be used on the contact surfaces of the phalanges for detecting pressure. These are relatively inexpensive and contribute to an inexpensive, yet functional, compliant hand. Wiring to a remote data acquisition device can be accomplished using conductive thread commonly used for electronics integration in clothing; this prevents sensor wiring from affecting the joint stiffnesses. Together these options provide an underactuated finger design which has robust sensing capabilities suitable for sensing object shape and judging quality of grasp without necessarily resorting to computer vision. Future work may also include further friction testing to determine the optimal thickness of silicone to provide the best combination of friction and compliance properties on the finger surfaces. Extensive and more accurate testing of the future completed system will also be necessary.

Finger joint stiffnesses were an important part of the design problem. Selecting Nitinol cross sections and active wire lengths appropriately allows concurrent synchronized motion in all the joints during the free phase of grasping and a more natural grasping motion with uniform

rate of closure. A default-closed pre-form of the joints also allows a single-cable actuation, simplifying the design. Due to a manufacturing imperfection of the plate and excessive stiffness limiting the articulation of the joints, the first prototype did not attain the expected purpose. By rectifying these parameters, a second more fully functional prototype has been designed. Not only did benchtop testing prove the basic functionality of the finger but also highlighted interesting results for the values of torque in the respective joints. Inaccuracy compared to expectations motivated 3-point bending tests to verify the assumed value of Young's modulus for the Nitinol. The inaccuracy previously observed decreased respectively to 63% to 53% for the MCPJ. Besides doing these experiments more accurately, the inaccuracy could also be lowered by verifying the value of the diameter of the Nitinol joints, if it is different from the manufacturer's stated value.

Also, grasping abilities were improved by increasing the thickness of the silicone pads at the fingertips. Indeed, friction testing showed noticeable improvements by increasing the thickness from 0.004" to 0.008". On this aspect of the finger design, complementary tests need to be performed, to measure friction on irregularly shaped objects, in order to demonstrate whether improved contact is valid not only on flat surfaces.

Characterization of the interface between PMMA and Nitinol using two different techniques showed relatively good maximum values of adhesive strength for non-treated samples. The values are even comparable to the ones obtained with specially treated samples (using coupling agents or texture modifications). The future possibility exists for using polymeric materials with Nitinol in robotic hands. In this type of case, the work presented in this thesis may serve as a set of design guidelines.

References

[1] M. Grebenstein, A. Albu-Schaffer, T. Bahls, M. Chalon, O. Eiberger, O. Friedl, R. Gruber, S. Haddadin, U. Hagn, R. Haslinger, H. Hoppner, S. Jörg, M. Nickl, A. Nothelfer, F. Petit, J. Reill, N. Seitz, T. Wimbock, S. Wolf, T. Wusthoff and G. Hirzinger , "The DLR Arm System," in *IEEE International Conference on Robotics and Automation*, Shanghai, China, 2011, pp. 3175-3182.

[2] J. Buttterfass, M. Grebenstein, H. Liu and G. Hirzinger , "DLR-Hand II: Next Generation of a Dexterous Robot Hand," in *IEEE International Conference on Robotics and Automation*, Seoul, Korea, 2001, pp. 3175-3182.

[3] The Shadow Robot Company, "Shadow Dexterous Hand C6M2 Technical Specification," 2012. [Online]. Available: http://www.shadowrobot.com/downloads/. [Accessed January 2013].

[4] S. C. Jacobsen, E. K. Iversen , D. F. Knutti, R. T. Johnson and K. B. Biggers, "Design of the Utah-M.I.T Dexterous Hand," vol. 3, Center of ENgineering Design, University of Utah, 1986, pp. 1520-1532.

[5] I. Spectrum, "Dean Kamen's "Luke Arm" Prosthesis Readies for Clinical Trials," [Online]. Available: http://spectrum.ieee.org/biomedical/bionics/dean-kamens-luke-arm-prosthesis-readies-for-clinical-trials. [Accessed 1 August 2013].

[6] P. Rea, "On the Design of Underactuated Finger Mechanisms for Robotic Hands," in *Advances in Mechatronics*, 2011, pp. 131-154.

[7] R. Balasubramanian and A. M. Dollar, "Performance of Serial Underactuated Mechanisms: Number of Degrees of Freedom and Actuators," in *IEEE INternational Conference on Intelligent Robots and Systems*, 2011, pp. 1823-1829.

[8] N. Fukaya , S. Toyama, T. Asfour and R. Dillman , "Design of the TUAT/Karlsruhe Humanoid Hand," in *IEEE Internatinal Conference on Intelligent Robots and Systems*, vol. 3, 2000, pp. 1754-1759.

[9] M. Rakic, "Multifingered Robot Hand with Self Adaptibility," in *Robotics and Computer-integrated Manufacturing*, vol. 3, 1989, pp. 269-276.

[10] J. D. Crisman, C. Kanojia and I. Zeid, "Graspar: a Flexible, Easily Controllable Robotic Hand," in *IEEE Robotixs and Automation Magazine* , 1996, pp. 32-38.

[11] A. M. Dollar and R. D. Howe, "The Highly Adaptive SDM Hand: Design and Performance Evaluation," in *The International Journal of Robotics Research*, vol. 29, 2010, pp. 585-597.

[12] L. Birglen and C. M. Gosselin, "Optimal Design of 2-Phalanx Underactuated Fingers," in *International Conference on Intelligent Manipulation and grasping* , Genoa, Italy, 2004, pp. 110-116.

[13] H. Nakamoto, F. Kobayashi, N. Imamura and H. Shirasawa, "universal Robot Hand Equipped with Tactile and joint Torque Sensors - Development and Experiments on Stifness Control and Object Recognition," in *Systemics, Cybernetics and Informatics*, vol. 5, pp. 79-84.

[14] "Degrees of freedom (mechanics)," [Online]. Available:

http://en.wikipedia.org/wiki/Degrees_of_freedom_(mechanics). [Accessed Avril 2013].

[15] R. Olfati-Saber, "Nonlinear Control of Underactuated Mechanical Systems with Application to Robotics and Aerospace Vehicles," in *Ph.D Thesis, Department of Electrical ENgineering and Computer Science,* Massachusetts Institute of Technology, Cambridge, MA, February 2001.

[16] NASA, "Robonaut," [Online]. Available: http://robonaut.jsc.nasa.gov/default.asp. [Accessed Avril 2013].

[17] H. Liu, K. Wu, P. Meusel, Hirzinger G, M. Jin, Y. Liu, S. Fan, T. Lan and Z. Chen, "A dexterous Humanoid Five-fingered Robotic Hand," in *Proceedings of the 17th IEEE International Symposium on Robot and Human Interactive Communication, Technische Universität München,* Munich, Germany, 2008, pp. 371-376.

[18] T. Laliberté, L. Birglen and C. M. Gosselin, "Underactuation in Robotic Grasping Hands," in *Machine Intelligence & Robotic Control,* vol. 4, 2002, pp. 1-11.

[19] S. Nasser , D. Rincon and M. Rodriguez , "Design of an Anthropomorphic Underactuated Hand Prostehesis with Passive-Adaptive Grasping Capabilities," in *Florida Conference on Recent Advances in Robotics (FCRAR),* 2006, pp. 1-7.

[20] A. Stefan , J. Spanjer , R. Balasubramanian, A. M. Dollar and J. L. Herder, "Underactuated gripper that is Able to Convert from Precision to Power Grasp by a Variable transmission ratio," in *Advances in Reconfigurable Mechanisms and Robots I,* J. S. Dai and al., Eds., Springer, 2012.

[21] A. M. Dollar, L. P. Jentoft, J. H. Gao and R. D. Howe, "Contact Sensing and Grasping

Performance of Compliant Hands," in *Autonomous Robots*, vol. 28, 2010, pp. 65-75.

[22] L. L. Howell, "Compliant Mechanisms," John Wiley & Sons, 2001.

[23] G. Figliolini and P. Rea, "Overall design of Ca.U.M.Ha robotic hand," in *Robotica*, 2006, pp. 329-331.

[24] "Polymethyl methacrylate," [Online]. Available: http://fr.wikipedia.org/wiki/Polym%C3%A9thacrylate_de_m%C3%A9thyle. [Accessed 30 Mars 2013].

[25] G. B. Kauffman and I. Mayo, "The story of Nitinol: The Serendipitous Discovery of the Memory Metal and Its Applications," in *The Chemical Educator*, 1996, pp. 1-21.

[26] L. Petrini and F. Migliavacca , "Biomedical Applications of Shape Memory Alloys," in *Journal of Metallurgy*, 2011, pp. 1-15.

[27] Duerig, Pelton and Stoeckel, "An Overview of Nitniol Medical Applications," in *Material Science and Engineering A273-275*, 1999, pp. 149-160.

[28] A. Falvo, "Thermomechanical characterization of Nickel-Titanium Shape Memory Alloys," in *Doctoral Course on Mechanical Engineering*, Thesis submitted for the degree Doctor of Philiosophy in Mechanical Engineering , pp. 1-128.

[29] Stoeckel and Yu, "Superelastic NiTi Wire," in *Wire Journal International* , 1991, pp. 45-50.

[30] Johnson Matthey Medical Components, "Nitinol Technical Properties," [Online]. Available: http://jmmedical.com/resources/221/Nitinol-Technical-Properties.html.

[Accessed 05 June 2013].

[31] K. Otsuka and C. M. Wayman, Shape Memory Materials, Cambridge University Press, 1999.

[32] "Types of modulus of Elasticity," 2010. [Online]. Available: http://www.tutorvista.com/content/physics/physics-iii/solids-and-fluids/elasticity-modulus.php. [Accessed 12 June 2013].

[33] Memry, "Physical Properties of Nitinol," [Online]. Available: http://memry.com/nitinol-iq/nitinol-fundamentals/physical-properties. [Accessed 12 June 2013].

[34] Memry, "Fabrication & Heat treatment of Nitinol," [Online]. Available: http://memry.com/nitinol-iq/nitinol-fundamentals/fabrication-heat-treatment. [Accessed 26 06 2013].

[35] C. Ochoa-Putman and U. K. Vaidya, "Mechanisms of Interfacial Adhesion in Metal-Polymer Composites," pp. 1-6.

[36] "IR/Functional Group Laboratory Experiment," [Online]. Available: http://classes.kvcc.edu/chm220/IR/prelab/introduction.htm. [Accessed 11 June 2013].

[37] A. M. Goyzueta, "Passive and Actuated Grasping USing Superelastic Materials for Surgical Applications," in *Thesis presented to the faculty of the graduate college at the University of Nebraska in partial fulfillment of requirements for the degree of Master of Science, Mechanical Engineering and Applied Mechanics*, 2013.

[38] Pico Technology, "Experiment to Measure the Deflection of a Cantilever Beam," [Online]. Available: http://www.picotech.com/experiments/beam_deflection/. [Accessed

12 June 2013].

[39] B. O. Calcagno, K. R. Hart and W. C. Crone, "Adhesion Strength in Metal/Polymer Composites," in *Experimental and Applied Mechanics*, vol. 6, T. proulx, Ed., 2011, pp. 149-155.

[40] E. B, "Binding metals to polymers. A short review of basic physical mechansims," in *Journal de Physique IV, Colloque C7, suplément au Journal de Physique III*, nov 1993.

[41] "Solid surface energy data (SFE) for common polymers," [Online]. Available: http://www.surface-tension.de/solid-surface-energy.htm. [Accessed 30 Mars 2013].

[42] M. Romero, B. Chabert and A. Domard, "IR Spectroscopy Approach for the Study of Interactions Between an Oxidized Aluminium Poly(propylene-g-acrylic acid) Film," in *Journal of Applied Polymer Science*, 1993, pp. 543-554.

[43] K. Jonnalagadda, G. E. Kline and N. R. Sottos, "Local Displacements and Load Transfer in Shape Memory Alloy Composites," in *Experimental Mechanics*, 1997, pp. 78-86.

[44] L. S. Penn and S. M. Lee, "Interpretation of Experimental Results in the Single Pull-Out Filament Test," in *Journal of Composites Technology & Research* , 1989, pp. 23-30.

[45] J. Paine, W. Jones and C. Rogers, "Nitinol Actuator to Host Composite Interfacial Adhesion in Adaptive Hybrid Composite," in *33rd Structural Dynamics and Materials Conference*, 1992, pp. 556-565.

[46] N. Smith, G. Antoun, A. Ellis and W. Crone, "Improved Adhesion between Nickel–Titanium Shape Memory Alloy and a Polymer Matrix via Silane Coupling Agents," in *Composites: Part A 35*, 2004, pp. 1307-1312.

[47] "Friction," [Online]. Available: http://en.wikipedia.org/wiki/Friction. [Accessed 11 March 2013].

[48] B. O. Calcagno, C. Rinaldi, T. A. Osswald and Crone Wendy C, "Fracture Induced by Cold Rolling in metal/Polymer Composites," in *Proceedings of the SEM Annual COnference* , Albuquerque, New Mexico, 2009, pp. 1-8.

[49] P. Tiezzi, I. Kao and G. Vassura, "Effect of Layer Compliance on Frictional Behavior of Soft Robotic Fingers," in *Proceedings of the 2006 IEEE/RSJ International Conference on Intelligent Robots and Systems*, Beijing, China, 2006, pp. 4012-4017.

[50] L. Biagiotti, P. Tiezzi, G. Vassura and C. Melchiorri, "Modelling and Controlling the Compliance of a Robotic Hand with Soft Finger-pads," pp. 1-20.

[51] P. J. Blau, Friction Science and Technology, L. L Faulkner, 1996.

[52] H. -. Y. Han and S. Kawamura, "Analysis of Stiffness of Human Fingertip and Comparison with Artificial Fingers," in *IEEE Conference on Robotic on Systems, Man and Cybernetics*, 1999, pp. 800-805.

[53] J.-C. Liao and M. A. Srinivasan, "Experimental Investigation of Frictional Properties of the Human Fingerpad," M.I.T., Massachusetts, 1999.

[54] Albright Technologies Inc, [Online]. Available: http://albright1.com/types-and-properties/. [Accessed 1 August 2013].

[55] K. Neuking, A. Abu-Zarifa and G. Eggler, "Surface Engineering of Shape memor Alloy/Polymer composites: Improvement of the Adhesion between Polymers and Pseudoelastic Shape Memory Alloy," in *Material Science and Engineering A*, 2004, pp.

1307-1312.

[56] Neuking K, Abu-Zarifa A and Eggeler G, "Surface Engineering of Shape Memory Alloy/Polymer-Composites: Improvement of the Adhesion between Polymers and Pseudoelastic Shape Memory Alloys," in *Materials Science and Engineering A*, 2008, pp. 606-611.

[57] K. Torabi, "Fourier Transform Infrared Spectroscopy in Size Inclusion Chromatography," in *Thesis submitted for the Degree of Master of Applied Chemistry*, university of Toronto, 1999.

[58] University of Cambridge, "Micrograph 771 and full record," [Online]. Available: http://www.doitpoms.ac.uk/miclib/micrograph_record.php?id=771. [Accessed 03 Juillet 2013].

Appendix

Appendix A: Commercial survey

A survey of commercially available cross sections for Nitinol wires and ribbons elucidated design options for different maximum grasp forces. In particular, wire diameter can be varied (larger diameters producing stiffer joints for the same active beam length) or the cross section shape can be changed. Several examples are given in the following table.

D = 1.02 mm			
Joint	**Torque (N.m)**	**Active length of Nitinol (mm)**	**Curvature radius (mm)**
MCPJ	0.46	4.45	2.83
PIPJ	0.27	7.58	7.58

Rectangular cross section (ribbon): b = 3.6 mm, h = 0.66 mm, $I = \frac{b.h^3}{12}$			
Joint	**Torque (N.m)**	**Active length of Nitinol (mm)**	**Curvature radius (mm)**
MCPJ	0.46	7.32	4.66
PIPJ	0.27	12.48	7.94

Rectangular cross section (ribbon): b = 3.556 mm, h = 0.635 mm, $I = \frac{b.h^3}{12}$			
Joint	**Torque (N.m)**	**Active length of Nitinol (mm)**	**Curvature radius (mm)**
MCPJ	0.46	6.44	4.10
PIPJ	0.27	10.97	6.99

Appendix B: Young's modulus calculation

Test #1			
Mass (Kg)	Deflection y (mm)	Deflection y (m)	Young's Modulus (Pa)
0,05	4,55	4,55E-03	1,575E+10
	4,46	4,46E-03	1,607E+10
	4,54	4,54E-03	1,579E+10
	4,69	4,69E-03	1,528E+10
	4,57	4,57E-03	1,568E+10
Average	*4,56*	*4,56E-03*	*1,571E+10*
Std. Dev.	*0,08*	*8,29E-05*	*2,833E+08*
	y = 4,56 ± 0,08 mm		E = 15,71 ± 0,28 Gpa

Test #2			
Mass (Kg)	Deflection y (mm)	Deflection y (m)	Young's Modulus (Pa)
0,10	7,93	7,93E-03	1,808E+10
	7,36	7,36E-03	1,947E+10
	6,98	6,98E-03	2,054E+10
	7,53	7,53E-03	1,904E+10
	7,67	7,67E-03	1,869E+10
Average	*7,49*	*7,49E-03*	*1,916E+10*
Std. Dev.	*0,36*	*3,55E-04*	*9,227E+08*
	y = 7,49 ± 0,36 mm		E = 19,16 ± 0,92 Gpa

Test #3			
Mass (Kg)	Deflection y (mm)	Deflection y (m)	Young's Modulus (Pa)
0,15	10,44	1,04E-02	2,059E+10
	10,16	1,02E-02	2,116E+10
	9,48	9,48E-03	2,268E+10
	10,21	1,02E-02	2,106E+10
	10,48	1,05E-02	2,052E+10
Average	*10,15*	*1,02E-02*	*2,120E+10*
Std. Dev.	*0,40*	*4,02E-04*	*8,727E+08*
	y = 10,15 ± 0,40 mm		E = 21,2 ± 0,9 Gpa

Test #4			
Mass (Kg)	Deflection y (mm)	Deflection y (m)	Young's Modulus (Pa)
0,20	12,32	1,23E-02	2,327E+10
	11,53	1,15E-02	2,486E+10
	11,56	1,16E-02	2,480E+10
	11,75	1,18E-02	2,440E+10
	12,19	1,22E-02	2,352E+10
Average	*11,87*	*1,19E-02*	*2,417E+10*
Std. Dev.	*0,36*	*3,64E-04*	*7,359E+08*
	y = 11,87 ± 0,36 mm		E = 24,17 ± 0,74 Gpa

Test #5			
Mass (Kg)	Deflection y (mm)	Deflection y (m)	Young's Modulus (Pa)
0,24	17,84	1,78E-02	1,928E+10
	16,23	1,62E-02	2,120E+10
	16,02	1,60E-02	2,147E+10
	17,25	1,73E-02	1,994E+10
	17,88	1,79E-02	1,924E+10
Average	*17,04*	*1,70E-02*	*2,023E+10*
Std. Dev.	*0,88*	*8,78E-04*	*1,053E+09*
	y = 17,04 ± 0,88 mm		E = 20,23 ± 1,05 Gpa

Appendix C: Overall Young's modulus calculation

Test #	Mass (Kg)	Weight	E (Pa)	E average
Test #1	0,05	0,125	1,58E+10	1,57E+10
			1,61E+10	
			1,58E+10	
			1,53E+10	
			1,57E+10	
Test #2	0,1	0,250	1,81E+10	1,92E+10
			1,95E+10	
			2,05E+10	
			1,90E+10	
			1,87E+10	
Test #3	0,15	0,250	2,06E+10	2,12E+10
			2,12E+10	
			2,27E+10	
			2,11E+10	
			2,05E+10	
Test #4	0,2	0,250	2,33E+10	2,42E+10
			2,49E+10	
			2,48E+10	
			2,44E+10	
			2,35E+10	
Test #5	0,24	0,125	1,93E+10	2,02E+10
			2,12E+10	
			2,15E+10	
			1,99E+10	
			1,92E+10	
Sum	0,74	1,000		
Average			2,15E+10	2,06E+10
Std. Dev.			2,27E+09	2,8E+09
			Unweighted Average	Weighted Average
			E = 21,5 ± 2,3 Gpa	E = 20,6 ± 2,8 Gpa

Appendix D: Speed and power recommendations for materials

Section 12: Speed and Power Recommendations

30 Watt - Epilog Mini/Helix

	300 DPI RASTER ENGRAVING	400 DPI RASTER ENGRAVING	600 DPI RASTER ENGRAVING	VECTOR CUTTING
	SPEED/POWER	SPEED/POWER	SPEED/POWER	SPEED/POWER/FREQUENCY
Wood Cherry – Alder - Walnut	25/100	35/100	45/100	⅛" (3 mm) – 25/100/500 ¼" (6 mm) – 8/100/500 (multiple passes may allow cutting of thicker materials)
Acrylic	100/100	100/90	100/80	⅛" (3 mm) – 15/100/5000 ¼" (6 mm) – 5/100/5000 (multiple passes may allow cutting of thicker materials)
AlumaMark	80/40	80/35	80/30	N/A
Anodized Aluminum	100/90	100/80	100/70	N/A
Painted Brass	100/90	100/80	100/70	N/A
Marbleized Painted Brass	100/100	100/90	100/80	N/A
Corian Or Avonite	15/100	20/100	25/100	⅛" (3 mm) – 10/100/5000
Delrin Seals	100/90	100/80	100/70	30/100/500
Glass	15/100	20/100	25/100	N/A
Laserable Plastic	100/70	100/60	100/50	20/80/5000
Leather	100/65	100/55	100/45	⅛" (3 mm) - 40/90/500
Marble	10/100	15/100	20/100	N/A
Mat board	100/75	100/65	100/55	20/50/500
Melamine	30/100	40/100	50/100	N/A
Stainless Steel With Cerdec Coating	N/A	20/100	25/100	N/A
Rubber & Rubber Stamps	N/A	10/100	20/100	10/100/100

Appendix E: Product profile of the MED-2014

MED-2014

Silicone Dispersion

Product Profile

NuSil SILICONE TECHNOLOGY
Creative Partners in a Material World

NuSil Technology
1050 Cindy Lane • Carpinteria, CA 93013
805/684-8780 • 805/566-9905 Fax
www.nusil.com

An ISO 9001 Certified Company

Description

- Fully compounded, platinum-catalyzed, dimethyl-methylvinyl siloxane elastomers dispersed in xylene
- Heat-cured to form strong, thin, elastomeric films
- Excellent physical properties
- Usable life can be extended with refrigeration

Applications

- For fabricating variously shaped elastomeric parts by brushing, spraying, or dipping
- Used for making membranes or cast film

NuSil Technology's MED-2014 is a restricted products. It shall not be considered for use in human implantation for a period of greater than 29 days.

Typical Properties	Result	Metric Conv.	ASTM	NT-TM
Uncured:				
Appearance	Translucent	-	D2090	002
Viscosity	3,400 cP	3,400 mPas	D445	001
Non-Volatile Content	35%	-	D2288	004
Cured: 60 min. @ 50°C; 60 min. @ 150°C; Stabilize 3 hours minimum @ ambient temperature and humidity				
Specific Gravity	1.10	-	D792	003
Durometer, Type A	35	-	D2240	006
Tensile Strength	1,800 psi	12.4 MPa	D412, D882	007
Elongation	800%	-	D412, D882	007
Tear Strength, die B	185 ppi	33.6 k/Nm	D624	009

Instructions for Use

Thin MED-2014 to the desired consistency with xylene, the suggested solvent. Mix the material thoroughly before use. Achieve best results by filtering the dispersion appropriately before use. Take care to avoid solvent evaporation and air entrapment.

When using any solvent, always provide adequate ventilation and avoid skin contact. Follow manufacturer's label instructions and refer to appropriate MSDS.

The mold, mandrel, or part being coated with dispersion should be free from contamination, not inhibit the cure, and be able to withstand the cure cycle. Apply the dispersion by brushing, spraying, or dipping. Control the thickness by building up successive, thin (1-2 mil) coats. Allow the bulk of the solvent to evaporate between coats. When the desired thickness is obtained, set aside the coated object and allow the solvent to completely evaporate. Controlled low-humidity conditions will reduce bubbles while coating.

Packaging

1 Pint (450 g)
1 Gallon (3.6 kg)
5 Gallon (18.0 kg)

Warranty

3 Months

Caution

MED-2014 will cure in contact with most materials. Exceptions include butyl, latex, chlorinated rubbers, some RTV silicones, and unreacted residues of some curing agents.

Appendix F: Friction results for the 0.004" thick Silicone pad

Acrylic			Wood			Steel		
Test #1: 200g			Test #1: 200g			Test #1: 200g		
Mass Normal (g)	Mass Transv. (g)	Friction coeff.	Mass Normal (g)	Mass Transv. (g)	Friction coeff.	Mass Normal (g)	Mass Transv. (g)	Friction coeff.
200	250	1,25	200	190	0,95	200	150	0,75
	250	1,25		190	0,95		140	0,70
	240	1,20		200	1,00		150	0,75
	250	1,25		190	0,95		140	0,70
	220	1,10		170	0,85		150	0,75
Average	**242**	**1,21**	**Average**	**188**	**0,94**	**Average**	**146**	**0,73**
Std. Dev.	**13,0**	**0,07**	**Std. Dev.**	**11,0**	**0,05**	**Std. Dev.**	**5,5**	**0,03**
	μ = 1,21 ± 0,07 mm			**μ = 0,94 ± 0,05 mm**			**μ = 0,73 ± 0,03 mm**	
Test #1: 400g			**Test #1: 400g**			**Test #1: 400g**		
Mass Normal (g)	Mass Transv. (g)	Friction coeff.	Mass Normal (g)	Mass Transv. (g)	Friction coeff.	Mass Normal (g)	Mass Transv. (g)	Friction coeff.
400	450	1,13	400	390	0,98	400	340	0,85
	450	1,13		350	0,88		320	0,80
	470	1,18		350	0,88		340	0,85
	450	1,13		320	0,80		300	0,75
	450	1,13		330	0,83		300	0,75
Average	**454**	**1,14**	**Average**	**348**	**0,87**	**Average**	**320**	**0,80**
Std. Dev.	**8,9**	**0,02**	**Std. Dev.**	**26,8**	**0,07**	**Std. Dev.**	**20,0**	**0,05**
	μ = 1,14 ± 0,02 mm			**μ = 0,87 ± 0,07 mm**			**μ = 0,80 ± 0,05 mm**	
Test #1: 500g			**Test #1: 500g**			**Test #1: 500g**		
Mass Normal (g)	Mass Transv. (g)	Friction coeff.	Mass Normal (g)	Mass Transv. (g)	Friction coeff.	Mass Normal (g)	Mass Transv. (g)	Friction coeff.
500	550	1,10	500	420	0,84	500	370	0,74
	550	1,10		440	0,88		390	0,78
	520	1,04		450	0,90		350	0,70
	540	1,08		400	0,80		350	0,70
	540	1,08		400	0,80		370	0,74
Average	**540**	**1,08**	**Average**	**422**	**0,84**	**Average**	**366**	**0,73**
Std. Dev.	**12,2**	**0,02**	**Std. Dev.**	**22,8**	**0,05**	**Std. Dev.**	**16,7**	**0,03**
	μ = 1,08 ± 0,02 mm			**μ = 0,84 ± 0,05 mm**			**μ = 0,73 ± 0,03 mm**	

Appendix G: Friction results for the 0.008" thick Silicone pad

Acrylic		
Test #1: 400g		
Mass Normal (g)	Mass Transv. (g)	Friction coeff.
400	900	2,25
	770	1,93
	900	2,25
	900	2,25
Average	868	2,17
Std. Dev.	65,0	0,16
	μ = 2,17 ± 0,16 mm	

Wood		
Test #1: 200g		
Mass Normal (g)	Mass Transv. (g)	Friction coeff.
200	270	1,35
	250	1,25
	240	1,20
	220	1,10
	220	1,10
Average	240	1,2
Std. Dev.	21,2	0,1
	μ = 1,2 ± 0,1 mm	

Steel		
Test #1: 200g		
Mass Normal (g)	Mass Transv. (g)	Friction coeff.
200	350	1,75
	320	1,60
	310	1,55
	270	1,35
	340	1,70
Average	318	1,59
Std. Dev.	31,1	0,16
	μ = 1,59 ± 0,16 mm	

Wood		
Test #1: 400g		
Mass Normal (g)	Mass Transv. (g)	Friction coeff.
400	390	0,98
	350	0,88
	400	1,00
	400	1,00
	390	0,98
Average	386	0,97
Std. Dev.	20,7	0,05
	μ = 0,97 ± 0,05 mm	

Steel		
Test #1: 400g		
Mass Normal (g)	Mass Transv. (g)	Friction coeff.
400	620	1,55
	640	1,60
	640	1,60
	620	1,55
	620	1,55
Average	628	1,57
Std. Dev.	11,0	0,03
	μ = 1,57 ± 0,03 mm	

Wood		
Test #1: 500g		
Mass Normal (g)	Mass Transv. (g)	Friction coeff.
500	450	0,90
	530	1,06
	450	0,90
	550	1,10
	500	1,00
Average	496	0,99
Std. Dev.	45,6	0,09
	μ = 0,99 ± 0,09 mm	